Check for updates

JGR Space Physics

RESEARCH ARTICLE
10.1029/2026JA035434

Latitude Survey of Neutrons and Muons to Determine Cosmic Ray Neutron Sensing Yield Functions

Lasse Hertle[1,2], Fraser Baird[3], Ulrich Schmidt[2], Bernd Heber[4], Michael Walter[5], Nora Krebs[6,7], Paul Schattan[6,7], Pauli Väisänen[8], Peter Dietrich[1], Steffen Zacharias[1], Solveig Landmark[1], Daniel Rasche[1,9], Marco Kossatz[5], Gary Womack[10], Steve Hamann[10], Enrico Gazzola[11], and Martin Schrön[1]

[1]Helmholtz Centre for Environmental Research, Leipzig, Germany, [2]Physikalisches Institut, University Heidelberg, Heidelberg, Germany, [3]Surrey Space Centre, University of Surrey, Guildford, UK, [4]Institut für Experimentelle und Angewandte Physik, Christian-Albrechts-Universität zu Kiel, Kiel, Germany, [5]Deutsches Elektronen-Synchrotron, Zeuthen, Germany, [6]Department of Geography, University of Innsbruck, Innsbruck, Austria, [7]Institute of Hydrology and Water Management (HyWa), University of Natural Resources and Life Sciences (BOKU), Vienna, Austria, [8]Sodankylä Geophysical Observatory, University of Oulu, Oulu, Finland, [9]GFZ Helmholtz Centre for Geosciences, Potsdam, Germany, [10]Quaesta Instruments, Tucson, AZ, USA, [11]Finapp S.P.A., Padova, Italy

Abstract Cosmic Ray Neutron Sensing (CRNS) is a ground-based technique that utilizes epithermal neutron measurements as a proxy for environmental hydrogen content. Similarly to other ground-based cosmic ray detectors (e.g., neutron monitors), CRNS detectors are affected by the solar cycle and space weather events. Typically, these effects must be corrected, but CRNS detectors have also been specifically used to observe space weather. The specific sensitivity of CRNS detectors to the primary spectrum and the relationship to other cosmic ray measurements is not fully understood. A latitude survey was undertaken during the maximum of solar cycle 25, utilizing a mini neutron monitor, two CRNS detectors of different design and a muon telescope onboard the German Research Vessel Polarstern. The observations are presented and used to derive differential response functions and yield functions for two neutron detectors. While the differential response, between neutron detectors is similar, it strongly deviates between muon and neutron detectors.

Plain Language Summary Cosmic Ray Neutron Sensing (CRNS) is a ground-based technique to monitor the amount of hydrogen present in the local environment, such as soil moisture. It works by detecting low energy neutrons which are produced by cosmic rays interacting with earth's atmosphere and surface. Like other ground-based cosmic ray measurements, CRNS detectors are influenced by the solar cycle and space weather. These influences are usually removed from CRNS data, but CRNS detectors can also be used specifically for space weather observation. It is not fully understood how sensitive CRNS detectors are to various cosmic ray energies. A measurement campaign observing cosmic ray neutrons and muons was carried out at the peak of solar cycle 25. The campaign covered a large range of geomagnetic cut-off rigidity. The data collected is used to determine the sensitivity of the different cosmic rays detectors to cosmic rays of various energies. Overall, the neutron detectors show similar sensitivity while the muon observations deviate.

Key Points:

- Latitude survey utilizing neutron and muon detectors during solar maximum
- Similar yield function determined for epithermal neutron detectors and mini neutron monitor
- Muons and neutrons show significantly different sensitivity to primary cosmic rays

Supporting Information:

Supporting Information may be found in the online version of this article.

Correspondence to:

L. Hertle,
lasse.hertle@ufz.de

Citation:

Hertle, L., Baird, F., Schmidt, U., Heber, B., Walter, M., Krebs, N., et al. (2026). Latitude survey of neutrons and muons to determine cosmic ray neutron sensing yield functions. *Journal of Geophysical Research: Space Physics*, *131*, e2026JA035434. https://doi.org/10.1029/2026JA035434

Received 31 MAR 2026
Accepted 22 JUL 2026

Author Contributions:

Conceptualization: Lasse Hertle, Bernd Heber, Michael Walter, Paul Schattan, Martin Schrön
Data curation: Lasse Hertle, Fraser Baird, Bernd Heber, Michael Walter, Martin Schrön
Formal analysis: Lasse Hertle, Fraser Baird, Ulrich Schmidt, Steffen Zacharias, Daniel Rasche, Martin Schrön
Funding acquisition: Peter Dietrich, Steffen Zacharias, Martin Schrön
Investigation: Lasse Hertle, Fraser Baird, Michael Walter, Nora Krebs, Pauli Väisänen, Daniel Rasche, Martin Schrön

© 2026 The Author(s). Journal of Geophysical Research: Space Physics published by Wiley Periodicals LLC on behalf of American Geophysical Union. This is an open access article under the terms of the Creative Commons Attribution License, which permits use, distribution and reproduction in any medium, provided the original work is properly cited.

1. Introduction

Ground-based cosmic ray neutron and muon detectors have been in use for decades to study space weather, solar physics, and radiation impact on Earth. Neutron monitors especially have been used to provide continuous measurements of galactic cosmic rays and solar energetic particles since the early 1950s (Väisänen et al., 2021). Increasingly, ground-based cosmic ray detection is also applied in other disciplines, notably hydrology. Cosmic Ray Neutron Sensing (CRNS) is a measurement technique to monitor environmental water content using cosmic ray neutrons (Andreasen et al., 2017; Köhli, 2025; Zreda et al., 2008). Detected neutron count rates serve as a proxy for hydrogen content in the local environment. Evaporation neutrons produced by primary and secondary cosmic ray interactions with nuclei in the soil or atmosphere are moderated primarily through elastic scattering with hydrogen nuclei, making the measured neutron intensity inversely related to the amount of hydrogen present (Köhli et al., 2015). In contrast to neutron monitors, CRNS detectors do not include materials of high atomic number (e.g., lead) that have the potential to function as sources of secondary neutron production. Instead, hydrogen-rich moderating materials, such as polyethylene, are utilized to optimize the instruments sensitivity for epithermal neutrons (Köhli et al., 2018). In order to accurately monitor soil moisture, CRNS count rates need to be

21699402, 2026, 8, Downloaded from https://agupubs.onlinelibrary.wiley.com/doi/10.1029/2026JA035434 by Cochraneltalia, Wiley Online Library on [21/08/2026]. See the Terms and Conditions (https://onlinelibrary.wiley.com/terms-and-conditions) on Wiley Online Library for rules of use; OA articles are governed by the applicable Creative Commons License

Methodology: Lasse Hertle, Bernd Heber, Michael Walter, Paul Schattan, Martin Schrön
Project administration: Bernd Heber, Peter Dietrich, Solveig Landmark, Martin Schrön
Resources: Lasse Hertle, Bernd Heber, Michael Walter, Nora Krebs, Paul Schattan, Pauli Väisänen, Solveig Landmark, Marco Kossatz, Gary Womack, Steve Hamann, Enrico Gazzola
Software: Lasse Hertle, Ulrich Schmidt, Pauli Väisänen
Supervision: Ulrich Schmidt, Peter Dietrich, Steffen Zacharias, Martin Schrön
Validation: Lasse Hertle
Visualization: Lasse Hertle, Fraser Baird, Martin Schrön
Writing – original draft: Lasse Hertle, Fraser Baird, Steffen Zacharias, Martin Schrön
Writing – review & editing: Lasse Hertle, Fraser Baird, Ulrich Schmidt, Bernd Heber, Michael Walter, Nora Krebs, Paul Schattan, Pauli Väisänen, Peter Dietrich, Steffen Zacharias, Solveig Landmark, Daniel Rasche, Marco Kossatz, Gary Womack, Steve Hamann, Enrico Gazzola, Martin Schrön

corrected for changes in solar modulation, which is commonly done using either (a) neutron monitor data (Hertle et al., 2025; McJannet & Desilets, 2023) or (b) co-located muon detectors (Stevanato et al., 2022). A more in-depth explanation of both methods is provided in Appendix A. Both approaches face a similar challenge: the reference signal is not obtained from the same component of the cosmic ray shower. Neutron monitors contain lead, which acts as a producer, making them sensitive to high-energy cascade neutrons and secondary protons (Clem & Dorman, 2000). Additionally, there have been some differences observed during Forbush decreases between the response of neutron monitors and CRNS detectors (Hubert, 2024; McJannet et al., 2025; Schrön et al., 2024). In the case of muons observed differences are even larger. Epithermal neutrons are a result of neutron evaporation and moderation through the environment, whereas muons are primarily produced by the decay of mesons formed through cosmic ray spallation. Muon detectors are typically associated with higher median primary cosmic ray energies than neutron detectors (Poopakun et al., 2025). Accordingly, large differences have been found during space weather events between neutron and muon observations (McJannet et al., 2025; Riggi et al., 2025). Consequently, enhancing the correction of CRNS signals for solar modulation variations necessitates a more profound and quantitative comprehension of the CRNS detectors sensitivity to the primary cosmic ray spectrum. An improved understanding could also contribute to CRNS detectors being utilized as probes of space weather, despite their sensitivity to lower neutron energies (Baird et al., 2025; Hands et al., 2021; Riggi et al., 2025).

Latitude surveys, spanning a broad range of geomagnetic cut-off rigidities, allow the observation of a changing range of the primary cosmic ray spectrum. From the change of particle count rate with the change of geomagnetic cut-off rigidity a detector-specific yield function can be inferred which characterizes the sensitivity to the primary cosmic ray spectrum. There have been a number of latitude surveys done using neutron detectors with the vast majority of them utilizing a lead producer (Nagashima et al., 1989). Surveys utilizing lead-free neutron detectors are comparatively rare. To the best of our knowledge, six such surveys have been performed thus far: in 1976 (Stoker et al., 1980), in 1995 (Nuntiyakul et al., 2018), in 1996–1997 (Villoresi et al., 2000), in 2009–2010 (Nuntiyakul et al., 2020), in 2019–2020 (Hubert et al., 2026), and in 2023–2024 (Nuntiyakul et al., 2025). The latter was undertaken near the solar maximum; all others near or at solar minimum. The lead-free detectors employed in these studies were derived from neutron monitor designs and purpose-built for latitude surveys, or in one case Bonner Spheres. Consequently, differences in detector geometry, moderation materials, and moderator thickness reduce the comparability with relatively standardized lead-free neutron detectors commonly used in the scope of CRNS.

Against this background and in light of the fact that the response function of a detector is dependent on both the primary cosmic ray spectrum (Caballero-López & Moraal, 2012) and the variations in the spectrum over the course of the solar cycle (Potgieter, 2013), a more valid comparison of neutron detectors used in CRNS, neutron monitors and muon detectors is possible if they are included in the same survey. This study presents results from the first latitude survey combining CRNS detectors (Köhli et al., 2018; Stevanato et al., 2019), a mini neutron monitor (MNM) (Heber et al., 2015; Strauss et al., 2020), and muon detectors. The experiment was conducted during the maximum of solar cycle 25 onboard the German research icebreaker Polarstern (Hanfland & Cornish, 2025; Knust, 2017).

2. Methods

2.1. Measurement Campaign

In November 2024 two CRNS detectors, described below, were installed aboard the German ice-breaking Research Vessel (RV) Polarstern operated by the German Alfred Wegener Institute, Helmholtz Centre for Polar and Marine Research (Knust, 2017). One MNM and one muon telescope were already permanently installed on the same vessel. All detectors were installed within close proximity of each other, near the top of the vessel. The RV Polarstern set sail on the 23 November 2024 in Bremerhaven, Germany toward Antarctica and returned on the 14 April 2025. The RV Polarstern crossed southwards in the eastern South Atlantic Ocean, while the northbound journey was undertaken in the western South Atlantic Ocean. The full route and all visited ports are shown in Figure 1, alongside the apparent cut-off rigidity during the voyage. The cut-off rigidity quantifies the local shielding of the geomagnetic field. For every point on earth there can be a minimum particle rigidity value associated such that a particle is able to reach that point from space (e.g., Cooke et al., 1991). The apparent cut-off rigidity during the voyage ranges between 0 and 14.6 GV and was computed using the Open-Source

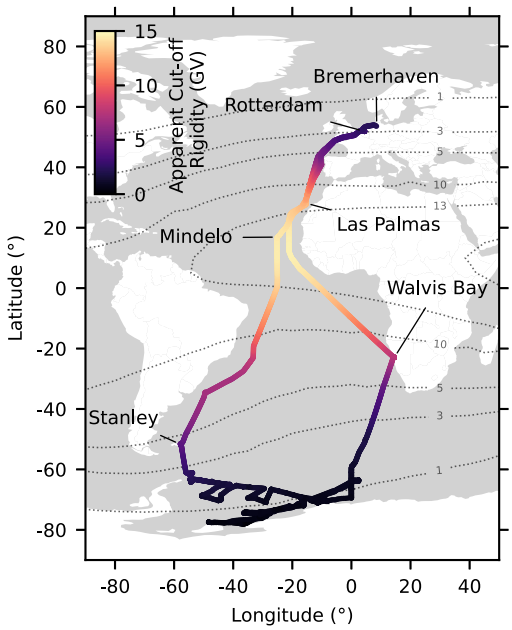


Figure 1. Track of the Research Vessel (RV) Polarstern between 23.11.2024 and 14.04.2025, with the apparent cut-off rigidity shown as a color scale. Cut-off rigidities not on the track of the Polarstern RV are shown as dotted contours, with the respective vertical cut-off rigidity annotated in GV. These have been computed in a 5° grid. All visited ports are annotated.

Geomagnetosphere Propagation Tool (OTSO), which performs particle trajectory tracing in the magnetosphere (for details see Larsen et al., 2023). Apparent cut-off rigidities were computed at three-hour intervals for the position of the Polarstern using the geomagnetic models IGRF 14 as well as Tsyganenko89 (Tsyganenko, 1989) and utilizing the Kp-Index as a measure of geomagnetic disturbance (Matzka, Stolle, et al., 2021). Additionally, a grid of vertical cut-off rigidities for the entire globe in 5° resolution has been computed for visualization purposes, utilizing only the IGRF 14 (given as Supporting Information S1).

The campaign is set in the maximum of solar cycle 25, during which the sunspot number showed a steady decline from its peak in summer of the 2024 (WDC-SILSO, Royal Observatory of Belgium, Brussels, https://doi.org/10.24414/qnza-ac80).

2.2. Detectors

CRNS detectors are not standardized to the same extent as neutron monitors. There are two different commonly used detection techniques: gas based ionization detectors and scintillator based detectors. Further, the material and thickness of shielding are not uniform across all CRNS detectors. As such, multiple detectors utilizing different detection techniques were included in the latitude survey.

2.2.1. Mini Neutron Monitor

The MNM, shown in Figure 2e, was installed in 2012 aboard the RV Polarstern (Heber et al., 2015) and is a compact neutron monitor whose core element is a ^{3}He-filled proportional counter (Strauss et al., 2020). Originally,



Figure 2. (a) Image of the Polarstern Research Vessel (Folke Mehrtens/Alfred-Wegener-Institut (CC-BY 4.0)), the position of all detectors is marked by an arrow. (b–e) Detectors utilized in the latitude survey.

21699402, 2026, 8, Downloaded from https://agupubs.onlinelibrary.wiley.com/doi/10.1029/2026JA035434 by Cochraneltalia, Wiley Online Library on [21/08/2026]. See the Terms and Conditions (https://onlinelibrary.wiley.com/terms-and-conditions) on Wiley Online Library for rules of use; OA articles are governed by the applicable Creative Commons License

21699402, 2026, 8, Downloaded from https://agupubs.onlinelibrary.wiley.com/doi/10.1029/2026JA035434 by Cochraneltalia, Wiley Online Library on [21/08/2026]. See the Terms and Conditions (https://onlinelibrary.wiley.com/terms-and-conditions) on Wiley Online Library for rules of use; OA articles are governed by the applicable Creative Commons License

it was designed to calibrate different neutron monitors (Moraal et al., 2000). The ^{3}He tube exploits the neutron-capture reaction $^3\mathrm{He} + \mathrm{n} \rightarrow {}^3\mathrm{H} + p + 0.76\,\mathrm{MeV}$ with a diameter of 51 mm and a length of 652 mm in which the released energy produces a well-defined ionization signal that is readily detected and discriminated against electronic noise. The ^{3}He counter is embedded in a cylindrical polyethylene moderator that thermalizes fast neutrons. The surrounding lead producer enhances the neutron yield through spallation reactions. The resulting detector assembly has a cylindrical geometry with a diameter of approximately 320 mm and a length of about 800 mm, and a total weight of roughly 250 kg (Walter et al., 2024). Details on the MNM design can be found in Strauss et al. (2020) and references therein.

2.2.2. CRNS–Quaesta Instruments

The Quaesta Instruments provided CRNS system, shown in Figure 2b, consists of a ^{3}He proportional counter, Neutron Pulse Module and DL2200 datalogger in a polyethylene box with 2.5 cm thick walls. Since the proportional counter exploits the same reaction as the MNM, the essential difference between them is to be found in the different thickness of polyethylene moderator and lack of lead producer, shifting the response of the detector to the epithermal neutron range. The neutron response function can be found in Millán-Callado et al. (2025).

2.2.3. CRNS–Finapp

The Finapp CRNS device, shown in Figure 2c, is a scintillator-based detector, made of Ag doped Zinc Sulfide, mixed with Lithium-6 Fluoride powder embedded in a silicone-based matrix. Lithium-6 provides the capture of thermal neutrons according to the reaction: $^6\mathrm{Li} + n \rightarrow {}^3\mathrm{H} + {}^4\mathrm{He} + 4.78\,\mathrm{MeV}$

The scintillator sheets are sandwiched with wavelength shifter slabs in a multilayer structure, encapsulated into a polyethylene moderator shield with a thickness of 15 mm, designed to shift the overall detection efficiency of the device to the epithermal range, with the highest response in the 1 eV–100 keV range. A simulated neutron response function can be found in Vykydal et al. (2025). Furthermore, the instrument is able to detect muons and electrons by discrimination of the temporal profile of the scintillator's light signal.

Unfortunately, any data taken by the Finapp instrument after 5 December 2024, was lost due to a corrupted storage medium. Therefore, only 12 days of data could be obtained from the Finapp CRNS.

2.2.4. Muon Telescope

The muon telescope, shown in Figure 2d, consists of two detector planes arranged one over the other at a distance of 50 cm. A plane contains 4 independent scintillator plates (25×25 cm^2 each). To suppress false signals, every scintillator plate is read out separately by two 4-channel photo-multipliers (Hamamatsu R5900U-00-M4). The 2×8 signals are processed by the data acquisition electronics to define the coincidence condition of the two signals of one scintillator. For a muon to be registered, coincidence between one scintillator of the upper plane and one scintillator of the lower plane is required, resulting in one of 16 possible directional combinations, of which 9 are unique. Due to the pitch, heave and roll of the vessel, this directional information is not used. Therefore, only the muon rate as the sum of all 16 coincidence combinations per hour is considered in this analysis.

2.3. Detector Response

The response of a ground-based cosmic ray particle detector can be thought of in two ways. First, the detector is sensitive to a specific energy range of particles that are directly measured. For a CRNS detector these would be epithermal neutrons. Second, the detector is sensitive to a specific part of the primary cosmic ray spectrum. The yield function of a detector quantifies the latter. Further, the detected signal then depends on the primary cosmic ray spectrum. The primary cosmic ray spectrum is mainly composed of protons and alpha particles but also contains heavier nuclei (Simpson, 1983). For each particle species a yield function informs how sensitive the detector is to differing energies of that particle. The primary cosmic ray spectrum is subject to changes over the solar cycle (Moraal, 2013), with lower rigidity particles generally most affected. The count rate N, dependent on cut-off rigidity R_c, of a particle detector can be described as the combination of yield function and cosmic ray spectrum, summed over all particle species (Clem & Dorman, 2000):

$$N(R_c, x, \phi) = \sum_i \int_{R_c}^{\infty} Y_i(R, x)\, j_i(R, \phi)\, \mathrm{d}R\,. \tag{1}$$

Here, Y_i is the yield function, dependent on particle rigidity R and atmospheric depth x (Mishev et al., 2020). The primary cosmic ray spectrum for each cosmic ray species is j_i. The primary spectrum is dependent on solar activity and can be approximated through the Force-Field approximation of the Parker Transport Equation (see e.g. a review by Moraal, 2013). The Force-Field approximation relates the local primary cosmic ray spectrum to the local interstellar spectrum (Gleeson & Urch, 1973) through the solar modulation potential ϕ

$$j_i = j_{\mathrm{LIS},i}(E_{\mathrm{Kin}} + \Phi_i)\, \frac{E_{\mathrm{Kin}}(E_{\mathrm{Kin}} + 2m_i)}{(E_{\mathrm{Kin}} + \Phi_i)(E_{\mathrm{Kin}} + \Phi_i + 2m_i)}, \tag{2}$$

with $\Phi_i = \frac{eZ_i}{A_i}\phi$, where e is the electron charge, Z_i and A_i are the charge number and mass number of species i, respectively, and m_i is the cosmic ray rest mass per nucleon, and E_{Kin} the kinetic energy per nucleon. For the local interstellar spectrum $j_{\mathrm{LIS},i}$ a parametrization by (Vos & Potgieter, 2015) is utilized

$$j_{\mathrm{LIS},i} = 2.70\, C_i \frac{(E_{\mathrm{Kin}})^{1.12} c^2}{v^2} \left(\frac{E_{\mathrm{Kin}} + 0.67}{1.67}\right)^{-3.93}, \tag{3}$$

where E_{Kin} is given in GeV, v is the particle velocity, c is the speed of light and C_i is a coefficient introduced by Koldobskiy et al. (2019) to scale the proton spectrum for helium isotopes. The coefficient itself is dependent on the solar modulation parameter ϕ

$$C_{\mathrm{He}} = 4.3 \cdot 10^{-8}\, \phi^2 - 6.2 \cdot 10^{-7}\, \phi + 0.337\,. \tag{4}$$

The solar modulation ϕ is taken from Väisänen et al. (2026), which is determined with a root mean square error merit function method based on hourly NM data from 38 stations, hourly cut-off rigidity computations based on Tsyganenko (1989), yield function by Mishev et al. (2020) and LIS from Boschini et al. (2020).

2.4. Data Processing

As can be seen in Figure 3a, the MNM suffers from significant spiking. These short term increases may be caused by high frequency signals from other machinery operated abroad the Polarstern RV. Therefore, the reduction of outliers constitutes a critical component of data processing. For consistency, all data are processed as follows:

First, all counts exceeding a threshold of twice the median count rate below 1 GV apparent cut-off rigidity are removed. At this threshold the data lies outside of a physically realistic value range and can be assumed to represent large outliers. An exception to this would be a Ground Level Enhancement (GLE), but no GLEs were observed during the latitude survey (https://gle.oulu.fi/).

Second, the data are binned into 12-hr intervals. For each bin, the median is calculated, alongside the Poisson standard deviation σ_P of the median and the Gaussian standard deviation σ_G of the 12-hr bin. Now for each bin data within four Poisson standard deviations in both directions from the median are retained. While the count rate of a neutron detector follows a Poisson distribution, the spikes do not. Thus a window of $4\sigma_P$ retains the majority of Poisson distributed counts while rejecting non-Poisson distributed counts. The effectiveness of this method is demonstrated by the CRNS detectors. As they do not exhibit heavy spiking (see Figure 5), they are entirely unaffected by the $4\sigma_P$ threshold.

Third, in some bins the data are noisy to such an extent that the median lies outside a realistic value range and the second step is no longer effective. In order to remove these, the ratio of Poisson and Gaussian standard deviation is scrutinized. Poisson distributions approach a Gaussian form with increasing event rate. Therefore, for 12-hr bins and the count rate of the MNM the ratio of the Gaussian and Poisson standard deviation is expected to be near unity, the actual ratio σ_G/σ_P is shifted toward slightly higher values since variations in atmospheric parameters and drifts across rigidities are not captured by σ_P. Further, the variance introduced into a bin by heavy spiking is not captured by a Poisson distribution, but is captured by the Gaussian standard deviation of the bin. Therefore,

21699402, 2026, 8, Downloaded from https://agupubs.onlinelibrary.wiley.com/doi/10.1029/2026JA035434 by Cochraneltalia, Wiley Online Library on [21/08/2026]. See the Terms and Conditions (https://onlinelibrary.wiley.com/terms-and-conditions) on Wiley Online Library for rules of use; OA articles are governed by the applicable Creative Commons License

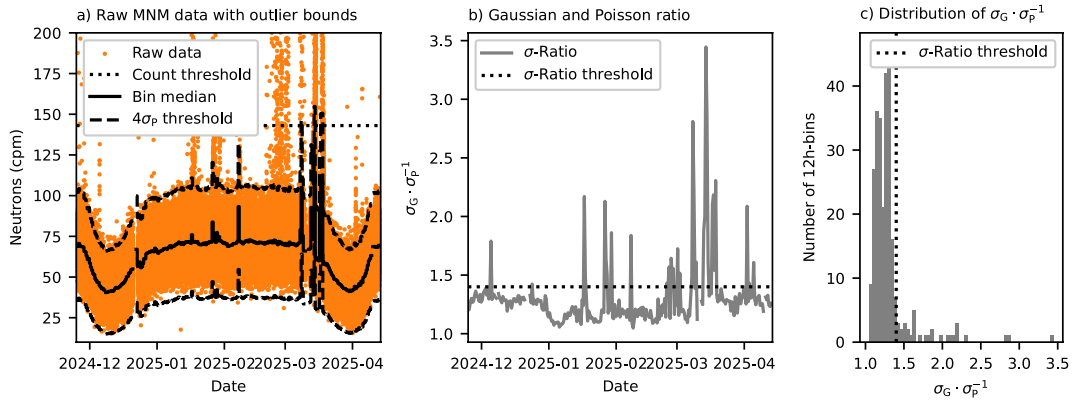


Figure 3. Outlier removal of the mini neutron monitor (MNM) data. (a) MNM raw data alongside the maximum count threshold and the $4\sigma_P$ threshold. (b) Ratio of Gaussian and Poisson standard deviation with the σ-ratio threshold. (c) The distribution of σ_G/σ_P with the σ-ratio threshold.

the ratio σ_G/σ_P increases significantly in such bins, as shown in Figure 3b. Thus, this ratio allows for discrimination of bins that include heavy spiking. It can be seen in Figure 3c that the distribution of the σ-Ratio is densely clustered between 1.0 and 1.4 and then abruptly declines. Therefore, all bins where the ratio σ_G/σ_P exceeds 1.4 are removed, approximately 11% of all bins.

In total, approximately 13% of the MNM data points have been removed, while no data points were removed from the count rates of all other detectors.

The count rates N_{observed} of all detectors have to be corrected for atmospheric changes, specifically pressure, temperature and humidity

$$N_{\text{corrected}} = N_{\text{observed}} \cdot C_p \cdot C_T \cdot C_h. \tag{5}$$

The correction factors C_P, C_T and C_h correct for pressure, temperature and humidity respectively. Not all detectors require all three corrections, if any correction is not required, the correction factor is set to 1. Since the detectors were mounted inside a climate controlled environment, atmospheric pressure, temperature and humidity were obtained from an external weather station aboard the RV Polarstern (Schmithüsen, 2026).

2.4.1. Atmospheric Pressure Correction

The influence of atmospheric pressure on secondary cosmic rays is well established theoretically (Dorman, 2004) and empirically (Cecchini & Spurio, 2012; Mendonça et al., 2019; Schrön et al., 2024). Commonly, the influence of atmospheric pressure is corrected using an exponential relation

$$C_P = e^{\beta(P-P_{\text{ref}})}, \tag{6}$$

with P being the atmospheric pressure and P_{ref} the reference pressure. β is the barometric coefficient. The effect of atmospheric pressure on secondary particle count rate is dependent on the energy of the secondary but also the primary producing particle's energy (Dorman, 2004). Therefore, the barometric coefficient is dependent on the cut-off rigidity of the measurement site and the current solar modulation of primary cosmic rays (Kobelev et al., 2011). Since the variations with the progressing solar cycle are minor and mostly visible over long time periods, they can be neglected in this work as the campaign spanned less than 6 months. In contrast, during the latitude survey the detectors passed through apparent cut-off rigidities between 0.0 and 14.6 GV, and are therefore susceptible to change in the barometric coefficient. For neutron detectors numerous formulas for the barometric coefficient have been proposed (Clem & Dorman, 2000; Desilets & Zreda, 2003; Dunai, 2000; Nuntiyakul et al., 2014; Tirado-Bueno et al., 2021), while we are only aware of one proposed barometric function for muons (Mendonça et al., 2019). All of these have been derived empirically from either latitude survey data or through a combination of identical, permanently installed stations at different cut-off rigidities.

21699402, 2026, 8, Downloaded from https://agupubs.onlinelibrary.wiley.com/doi/10.1029/2026JA035434 by Cochraneltalia, Wiley Online Library on [21/08/2026]. See the Terms and Conditions (https://onlinelibrary.wiley.com/terms-and-conditions) on Wiley Online Library for rules of use; OA articles are governed by the applicable Creative Commons License

Table 1
Pearson Correlation Coefficient Between Neutron and Muon Count Rates and Pressure for $R_C < 1$ GV

Method	Quaesta CRNS	MNM	Muon telescope
Uncorrected data	−0.947	−0.904	−0.617
Clem and Dorman (2000)	−0.143	−0.145	–
Dunai (2000)	0.038	−0.043	–
Desilets and Zreda (2003)	0.056	−0.031	–
Nuntiyakul et al. (2014)	−0.060	−0.111	–
Mendonça et al. (2019)	–	–	−0.383
Tirado-Bueno et al. (2021)	−0.032	−0.091	–
Fitted on data	−0.030	−0.090	−0.257

Note. The correlation coefficient is shown for both uncorrected and pressure corrected data utilizing different barometric coefficients.

As a consequence, the derived barometric coefficients are dependent on the sensitivity of the specific detector used. Therefore, their direct applicability to other detectors, with different particle energy sensitivity, is reduced. This is simply demonstrated by evaluating the Pearson correlation coefficient between the pressure corrected count rate utilizing different barometric coefficients and the atmospheric pressure. For reference, a constant barometric coefficient derived from the data itself is also included, alongside the uncorrected count rate. As atmospheric pressure correlates with latitude which in turn correlates with apparent cut-off rigidity, the comparison is only meaningful for $R_c < 1$GV, where the atmospheric cut-off exceeds the geomagnetic (Poluianov & Batalla, 2022).

Table 1 shows that all methods are able to remove the pressure dependence effectively. Yet, small differences between them remain discernible. The anti-correlation of the raw CRNS data to pressure is slightly higher than for the MNM data. One reason for this could be residual noise in the MNM signal. Another possible explanation lies in the neutron energy range the specific detectors are sensitive to. It is notable that the best and worst methods for each detector differs, while the data fitted approach performs comparatively well for both. A comparison at rigidities below 1 GV is not necessarily representative across rigidities. Additional uncertainties arise in this context. The different barometric functions presented above do not only disagree in parametrization but in their form being linear, logarithmic, exponential or polynomial. A choice of one functional shape might influence the scaling with rigidity. Therefore and due to the observed effectiveness below 1 GV, the constant data-derived coefficient is used for the neutrons, specifically $\beta_N = 0.00754$.

In the case of muons, the published method is also compared in Table 1 to a constant barometric coefficient derived from the data. Clearly, neither coefficient removes the pressure dependence as effectively as in the neutron case. However, the constant coefficient derived from the data is more effective. This might be again due to a difference in the muon detector's energy sensitivity. As with the neutrons the constant data-derived coefficient is used, $\beta_M = 0.0025$.

2.4.2. Atmospheric Temperature Correction

Atmospheric temperature also exhibits an influence on particle count rate in ground-based measurements. In contrast to atmospheric pressure, the effect of temperature on secondary neutrons is negligible (Dorman, 2004), therefore for all neutron measurements $C_T = 1$ is assumed. In contrast, there exists a pronounced temperature effect for muons (de Mendonça et al., 2016; Mendonça et al., 2019; Stevanato et al., 2022; Tanaka, 2025; Verpoest et al., 2024). The influence of atmospheric temperature is commonly corrected using the relation

$$C_T = (\vartheta(T - T_{\text{ref}}) + 1)^{-1}, \tag{7}$$

where T refers to atmospheric temperature, T_{ref} to the atmospheric temperature reference and ϑ is the thermal coefficient.

As observed for pressure, the temperature effect is also dependent on the primary particle spectrum. Again, the change of the temperature coefficient over time due to changes in solar modulation is negligible in this case. As with pressure, only one method has been proposed to derive the thermal coefficient from cut-off rigidity (Mendonça et al., 2019). Here again the benefit of a changing thermal coefficient with cut-off rigidity is outweighed by the difference in energy sensitivity between the detector used for deriving it and the detector installed on the RV Polarstern. Thus, a constant data-derived thermal coefficient is used with $\vartheta = 0.0026$.

As has been described above, both the barometric and thermal correction coefficients are dependent on cut-off rigidity. Therefore, utilizing constant barometric and thermal correction coefficients is an approximation and may impact the derived Dorman and Yield functions. A constant barometric coefficient can potentially lead to a slightly less steep Dorman function, as all proposed barometric functions increase with rigidity. Crucially, the intercomparability between the count rates is unaffected.

21699402, 2026, 8, Downloaded from https://agupubs.onlinelibrary.wiley.com/doi/10.1029/2026JA035434 by CochraneItalia, Wiley Online Library on [21/08/2026]. See the Terms and Conditions (https://onlinelibrary.wiley.com/terms-and-conditions) on Wiley Online Library for rules of use; OA articles are governed by the applicable Creative Commons License

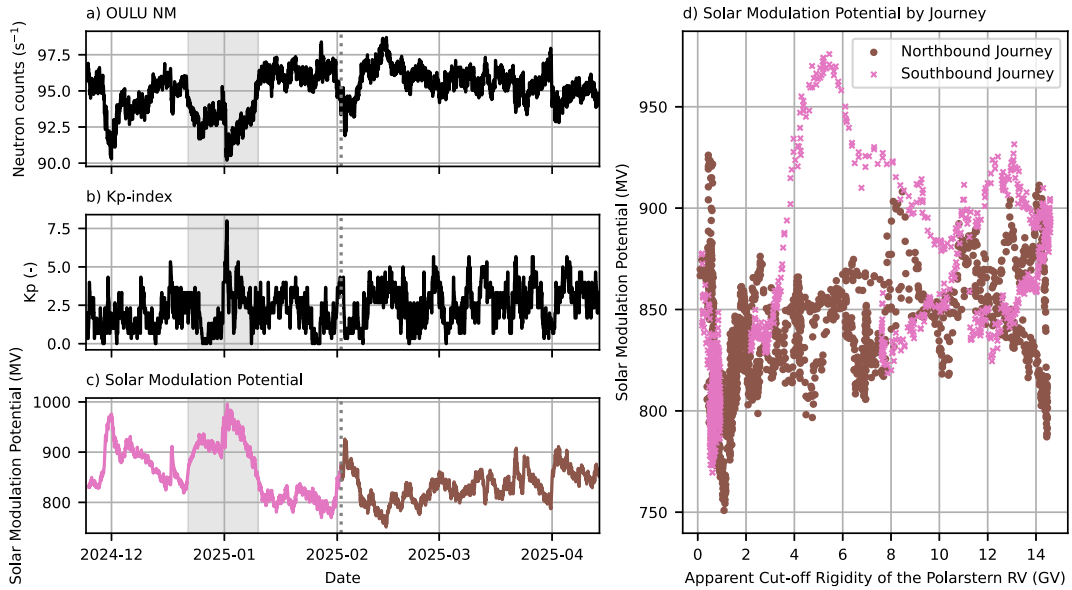


Figure 4. (a) Count rate of the Oulu neutron monitor, (b) Kp-Index and (c) solar modulation potential ϕ during the campaign. The split into southbound and northbound journey is marked as a grey dotted line. (d) Solar modulation potential shown against the apparent cut-off rigidity associated with the position of the Research Vessel Polarstern.

2.4.3. Atmospheric Humidity Correction

The effect of atmospheric humidity on epithermal neutrons is well established (Köhli et al., 2021; McJannet et al., 2025; Rosolem et al., 2013; Schrön et al., 2024). Therefore, a humidity correction is commonly applied (Bogena et al., 2022; Evans et al., 2016). The correction takes the shape (Rosolem et al., 2013):

$$C_h = (1 + 0.0054(h - h_{\text{ref}})) \tag{8}$$

where h refers to the absolute humidity and h_{ref} the reference absolute humidity. The correction factor was originally derived for CRNS detectors deployed over soil (Rosolem et al., 2013) and it has been demonstrated that the humidity correction is soil moisture dependent (Köhli et al., 2021). Yet, the original coefficient is still utilized since two separate deployments over water at different cut-off rigidities have demonstrated its effectiveness (McJannet et al., 2025; Schrön et al., 2024). An effect of water vapor on the count rates of neutron monitors has been suggested (Mangeard et al., 2018; Ruffolo et al., 2016) but a correction is not commonly applied, due to the much lower influence compared to epithermal neutrons. To be consistent with the standard corrections applied to data from neutron monitors the humidity correction is only applied to CRNS data, thus for all other detectors $C_{\text{h}} = 1$. However, for comparison with previous latitude surveys utilizing lead-free neutron monitors which are considerably more sensitive to epithermal neutrons, CRNS data is also shown without humidity correction.

2.4.4. Short Term Solar Modulation and Space Weather Events

To reduce the influence of space weather events on the observed reduction in count rate with rigidity, the Oulu neutron monitor was designated as a reference, alongside the Kp-Index as a measure of geomagnetic disturbance (Matzka, Stolle, et al., 2021). As shown in Figure 4 one strong Forbush decrease with geomagnetic disturbance occurred during the campaign. This event occurred during the southbound voyage approximately between 2.5 and 0 GV, it can also be readily observed in the CRNS Quaesta and MNM count rate in late December 2024, as shown in Figure 5. While the count rate during the Forbush decrease is shown for completeness in Figure 5, it has been removed from the data set for all subsequent analysis. The exact date range that has been removed is from 22 December 2024 until 10 January 2025 (marked grey in Figure 4).

Furthermore, the solar cycle maximum is characterized by rapid development of heliospheric conditions. This is particularly relevant as the campaign coincides with the expected polarity reversal of the Sun's southern hemisphere (Jha & Upton, 2024). In order to capture some of the heliospheric dynamics during the survey, the

21699402, 2026, 8, Downloaded from https://agupubs.onlinelibrary.wiley.com/doi/10.1029/2026JA035434 by Cochraneltalia, Wiley Online Library on [21/08/2026]. See the Terms and Conditions (https://onlinelibrary.wiley.com/terms-and-conditions) on Wiley Online Library for rules of use; OA articles are governed by the applicable Creative Commons License

21699402, 2026, 8, Downloaded from https://agupubs.onlinelibrary.wiley.com/doi/10.1029/2026JA035434 by Cochraneltalia, Wiley Online Library on [21/08/2026]. See the Terms and Conditions (https://onlinelibrary.wiley.com/terms-and-conditions) on Wiley Online Library for rules of use; OA articles are governed by the applicable Creative Commons License

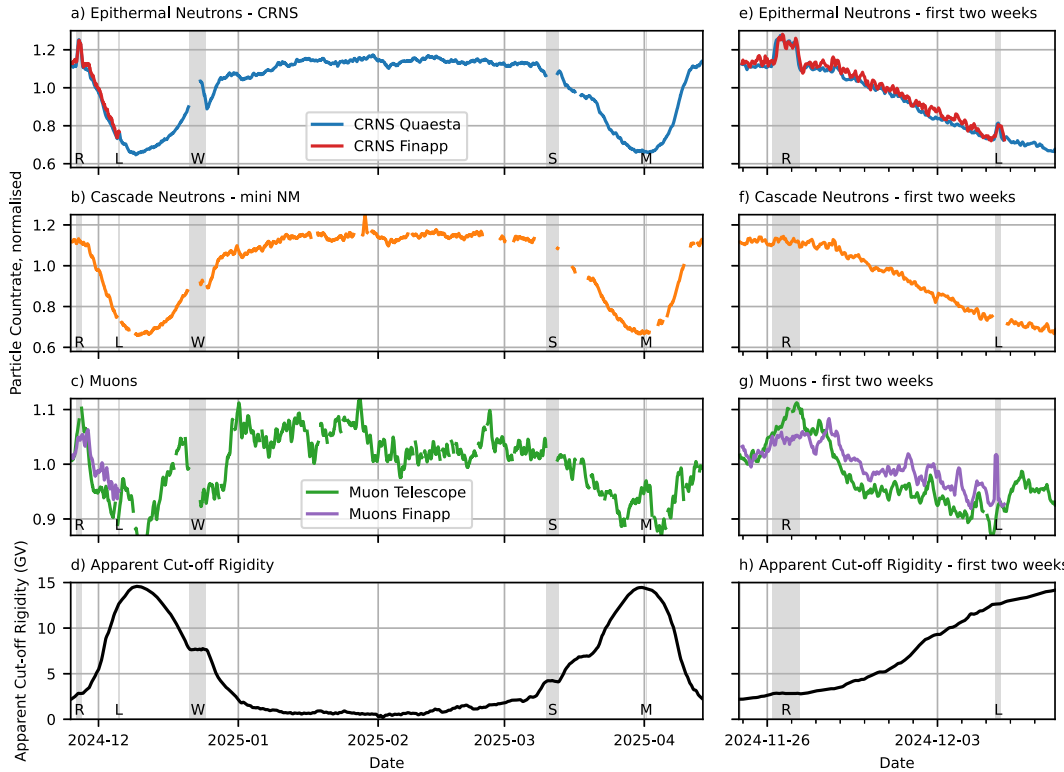


Figure 5. (a–c) Normalized count rates of all detectors, smoothed with a 12-hr rolling window. (e–g) Normalized count rates during the first 2 weeks of the campaign, smoothed with a 3-hr rolling window. (d), (h) Apparent cut-off rigidity associated with the position of the Research Vessel Polarstern. Time spent near land has been marked in grey and annotated with the initial letter of the respective port (R: Rotterdam, L: Las Palmas, W: Walvis Bay, S: Stanley, M: Mindelo).

campaign is split into a southbound and northbound voyage. The solar modulation potential during the southbound voyage exhibits a much larger variation than the during the northbound voyage.

3. Results

The count rates of all detectors are shown in Figure 5. All detectors exhibit a pronounced reaction to changes in apparent cut-off rigidity. The MNM and CRNS detectors show a relative reduction in count rate of approximately 40% over the course of the voyage. As expected, the muon detectors show a smaller reduction than the neutron detectors, with a maximum reduction of approximately 15%.

The two different CRNS techniques exhibit good agreement within the first 2 weeks. The Finapp CRNS shows higher variation, presumably due to a lower count rate, as the relative difference in variation is in-line with the Poisson standard deviation. In comparison, the discrepancy between the Finapp muon channel and the muon telescope is larger. While both detectors observe a similar trend, they frequently deviate from another. This is especially apparent during the Rotterdam port visit and immediately afterward (see Figure 5g). Here, the muon telescope shows a reduction in count rate approximately 12 hr before the Finapp muon channel.

Furthermore, as can be seen in Figure 5c, the rate distribution of the muon telescope shows significantly greater deviations compared to the more uniform neutron rate distributions. These cannot be explained by changes in apparent cut-off rigidity or by temperature or pressure influences. In particular, the anomalous increases in the count rate in mid-December 2024 and late March 2025 were not observed in previous years. Since there was no evidence of any external influence on the detector electronics during these periods, the cause of the signal fluctuations observed between December 2024 and March 2025 in the muon telescope remained unclear.

A clear and expected feature, that can be readily observed in Figure 5a, are elevated count rates in the CRNS detectors as the ship approaches the coast or lies in port. The phenomenon has been previously observed by Nuntiyakul et al. (2018, 2020) using lead-free neutron detectors, which are comparable in design to CRNS

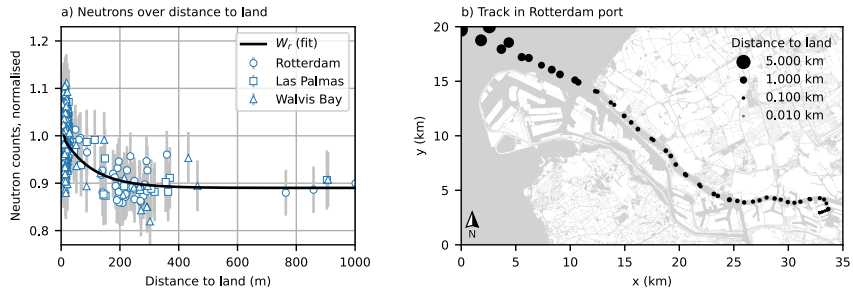


Figure 6. (a) Count rate of the Quaesta Cosmic Ray Neutron Sensing detector near the shore of three ports, with a function (W_r) of theoretical neutron contribution to the detector count rate over distance from Schrön et al. (2017). The visited ports are Rotterdam (The Netherlands), Las Palmas de Gran Canaria (Spain) and Walvis Bay (Namibia) (b) Map of the ship's track in the port of Rotterdam. Map data is taken from OpenStreetMap.

detectors. Elevated count rates are not observed in the MNM or in either muon detector, as can be seen in Figures 5b and 5c. This is expected as the neutrons detected by the MNM and CRNS do not share the same origin. Water holds comparatively low neutron evaporation potential in comparison to soil (Weimar, 2022). Furthermore, the hydrogen contained in water is an exceedingly effective neutron moderator. Thus, in the case of CRNS deployment over water it can be assumed that almost the entirety of the neutrons detected by the CRNS detector originates either in the atmosphere or in the steel construction of the ship (Weimar, 2022). As the ship approaches the shoreline, a growing number of albedo neutrons originating on dry land is able to reach the detectors. These albedo neutrons increase the CRNS count rate, but are unable to induce elevated counts in the MNM due to its thicker shielding. Since the MNM count rate does not increase it can be assumed that the neutrons produced in the MNM's lead by high energy protons and neutrons are the dominant source of counts and any albedo neutrons that are able to penetrate the shielding represent only a small fraction of the overall count rate. Therefore, neutrons originating in the local environment have little influence. The CRNS count rate over the distance to the nearest land is shown in Figure 6a for three visited ports, alongside an example of the ship's track in the port of Rotterdam. The CRNS count rate is reduced by approximately 10 % over a distance of 250 m from the shore, which is in line with the assumed CRNS footprint (Schrön et al., 2017, 2023). For further analysis all time spent in port or near the shore, marked grey in Figure 5, has been removed from the data.

The behavior of the detector count rates with changes in apparent cut-off rigidity characterizes the detector response. Figures 7a and 7b show the variation of particle count rates of all detectors as a function of apparent cut-off rigidity. The hourly count rates are fitted with the Dorman function (Clem & Dorman, 2000), which describes count rate as a function of cut-off rigidity:

$$N = N_0\left(1 - e^{-\alpha R_c^{-\kappa}}\right). \tag{9}$$

The fitted parameters alongside the fitting errors are shown in Table 2. The Finapp count rates are shown, but have not been fit because of the small amount of data due to above-mentioned reasons. The data from the muon telescope for the southbound route were likewise not analyzed due to the aforementioned signal fluctuations of unclear origin that occurred in December 2024. Given the strong anomalous signature, it was not possible to derive meaningful coefficients. The muon telescope data for the northbound route were analyzed; however, it should be noted that the fitting error of α remains more than an order of magnitude higher than that of the MNM and CRNS detector. This is likely due to an anomalous increase in counts in March 2025, which causes an increase of count rate at the highest rigidity and can be readily observed in Figure 5c. Another potential explanation is that the Dorman function was originally derived for neutron monitor measurements. Given the different dynamics of muon measurements with respect to cut-off rigidity, the data collected across the range of apparent cut-off rigidities span a comparatively smaller range of the muon Dorman function. This leads to a less defined function in comparison to neutron measurements. General statements about the shape of the muon telescope Dorman function can nevertheless be made. As shown in Figures 7a and 7b, the muon detector exhibits a much weaker modulation caused by increased rigidity compared to both neutron detectors. During the southbound journey the neutron detectors exhibit a nearly identical response, with only small deviations. The northbound journey shows a greater difference between the neutron detectors. The behavior of the neutron detectors below 1

21699402, 2026, 8, Downloaded from https://agupubs.onlinelibrary.wiley.com/doi/10.1029/2026JA035434 by Cochraneltalia, Wiley Online Library on [21/08/2026]. See the Terms and Conditions (https://onlinelibrary.wiley.com/terms-and-conditions) on Wiley Online Library for rules of use; OA articles are governed by the applicable Creative Commons License

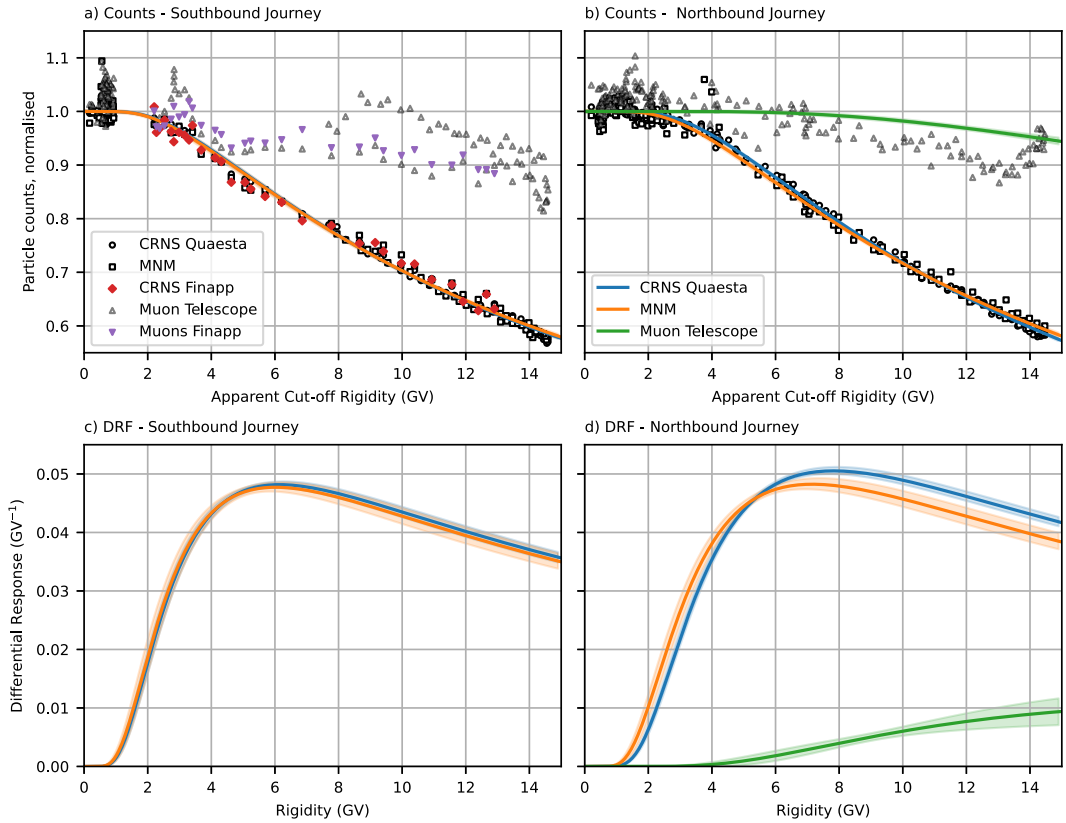


Figure 7. Normalized count rates of all detectors over apparent cut-off rigidity for the (a) southbound and (b) northbound journeys respectively. Points are scattered data in 12-hr resolution lines are Dorman functions fitted to the data in 1-hr resolution, the band indicates an error of 3σ of the fit. Differential response function for the three detectors that could be fit with a Dorman function for the (c) southbound and (d) northbound journey.

GV is well characterized, where the atmospheric cut-off is comparable to the magnetic cut-off (Poluianov & Batalla, 2022). As expected this is consistent between both journeys. For the muon telescope an analogous threshold is reached at a rigidity of approximately 4 GV, which has been reported previously in Carmichael et al. (1969).

From the Dorman function the Differential Response Function of each detector can be calculated

$$\mathrm{DRF} = -\frac{\mathrm{d}\ln N}{\mathrm{d}R} = \frac{\alpha\kappa R^{-\kappa-1}}{e^{\alpha R^{-\kappa}} - 1}. \tag{10}$$

Since the differential response function is independent of absolute particle counts it is ideal to compare the different detectors against each other, as shown in Figures 7c and 7d. It should be noted that the shape of the DRF

Table 2
Parameters of the Dorman Function (See Equation 9) Fitted to the Latitude Survey Data as Shown in Figures 7a and 7b

Journey	Detector	N_0 (s^{-1})	α (GV^{κ})	κ (−)
Southbound	MNM	1.182 ± 0.001	8.28 ± 0.20	0.834 ± 0.010
	Quaesta CRNS	1.938 ± 0.001	8.52 ± 0.14	0.847 ± 0.006
	Muon Telescope	–	–	–
Northbound	MNM	1.178 ± 0.001	10.42 ± 0.25	0.917 ± 0.010
	Quaesta CRNS	1.931 ± 0.001	12.24 ± 0.16	0.985 ± 0.005
	Muon Telescope	3.449 ± 0.002	26.9 ± 3.6	0.825 ± 0.052

21699402, 2026, 8, Downloaded from https://agupubs.onlinelibrary.wiley.com/doi/10.1029/2026JA035434 by Cochraneltalia, Wiley Online Library on [21/08/2026]. See the Terms and Conditions (https://onlinelibrary.wiley.com/terms-and-conditions) on Wiley Online Library for rules of use; OA articles are governed by the applicable Creative Commons License

21699402, 2026, 8, Downloaded from https://agupubs.onlinelibrary.wiley.com/doi/10.1029/2026JA035434 by Cochraneltalia, Wiley Online Library on [21/08/2026]. See the Terms and Conditions (https://onlinelibrary.wiley.com/terms-and-conditions) on Wiley Online Library for rules of use; OA articles are governed by the applicable Creative Commons License

is still dependent on the solar modulation, as changes in the primary spectrum are reflected in the Dorman function (Nuntiyakul et al., 2014). There is a large difference between the neutron and muon detectors. While the response for both neutron detectors peaks below 10 GV during both journeys, the muon telescope's response is still rising at 15 GV. This indicates that the peak response of the muon detector lies above the highest cut-off rigidity of the geomagnetic field. In contrast, the difference between the CRNS and MNM is much smaller, yet still significant. There is also a clear change between the southbound and northbound journeys. Both DRFs are shifted to slightly higher energies. Furthermore, the CRNS experiences a larger shift in comparison to the MNM. To characterize this behavior the peaks can be examined, during the southbound journey, the CRNS and MNM peak at 6.1 G and 6.0 GV respectively, while during the northbound voyage they peak at 7.8 and 7.2 GV. Simultaneously, the peak differential response also increases by 4.1% in the case of the CRNS and 0.8% for the MNM.

The Dorman function then can be used to derive the yield function for protons Y_H following the formalism of Caballero-López and Moraal (2012, Equation 18)

$$Y_H = -\frac{\mathrm{d}N}{\mathrm{d}R}\left(j_H(R) + 1.584\,F(R)\cdot j_{\mathrm{He}}(R)\right)^{-1}. \tag{11}$$

While Equation 1 contains a sum over all particle species, Equation 11 only contains hydrogen and helium explicitly, this is due the heavier nuclei having been absorbed into an effective scaling, contributing the factor of 1.584. The contributions of helium and hydrogen to the overall count rate are separated a parametrized double power law,

$$F(R) = 2\left(0.45^{1.4} + R^{1.4}\right)^{-10/1.4} R^{10}. \tag{12}$$

Further details on the derivation of these factors can be found in Caballero-López and Moraal (2012). While the Dorman functions and the DRF in Figure 7 were purely derived on the data collected during the Latitude survey, the derivation of a yield function necessitates a primary spectrum. The spectrum used is dependent on several choices, specifically the force-field approximation, j_{LIS} parametrization, and the derived modulation potential ϕ. Therefore, it should be noted that the derived yield function is not purely data-driven.

The hydrogen yield functions for the Quaesta CRNS detector and the MNM are shown in Figure 8a. A yield function for the CRNS detector without humidity is also shown for the northbound journey, as this processing step is not commonly observed in previous surveys. The non-humidity corrected CRNS yield shows a clear increase below 6 GV in comparison with the fully corrected CRNS. It is important to note, that the yield function is dependent on the actual count rate achieved by the detector. Comparisons should therefore be made utilizing normalized yield functions shown in Figures 8b–8d.

The normalized yield functions of the CRNS and MNM show almost exact agreement during the southbound journey, but diverge below approximately 5 GV during the northbound journey, which was to be expected given the results shown in Figure 7. Furthermore, there is a clearly observable difference between the journeys in both the CRNS and MNM yield functions.

The influence of the humidity correction can be clearly seen in Figure 8a. The CRNS yield function with and without humidity correction agree at higher rigidities but diverge below 5 GV. Below this point the yield function without humidity correction is comparatively increased. The yield function without humidity correction is only shown for the northbound journey, since the relative behavior on the southbound journey is the same.

The normalized yield functions are compared to previous latitude surveys in Figures 8b and 8c. For the MNM, the northbound yield function shows close agreement with the yield function derived by (Caballero-Lopez, 2016) and with a 3NM64 yield function based on (Nuntiyakul et al., 2018), while the southbound MNM diverges below 5 GV. For the Quaesta CRNS, comparison with previous non-leaded surveys (Nuntiyakul et al., 2018, 2020) shows general agreement above 5 GV. Below this threshold, the southbound CRNS and (Nuntiyakul et al., 2018) are consistent, while (Nuntiyakul et al., 2020) and the northbound CRNS diverge. Figure 8d includes a simulated CRNS yield function reported in Baird (2024). This yield function was computed by combining Geant4 simulations of a CRNS detector and its local environment (silica soil, 40% volumetric soil moisture) with the Model of Atmospheric Ionising Radiation Effects (MAIRE), (Hands et al., 2022; Lei et al., 2004). Clear discrepancies between the modeled yield function and those derived in this work are apparent. The most significant difference is

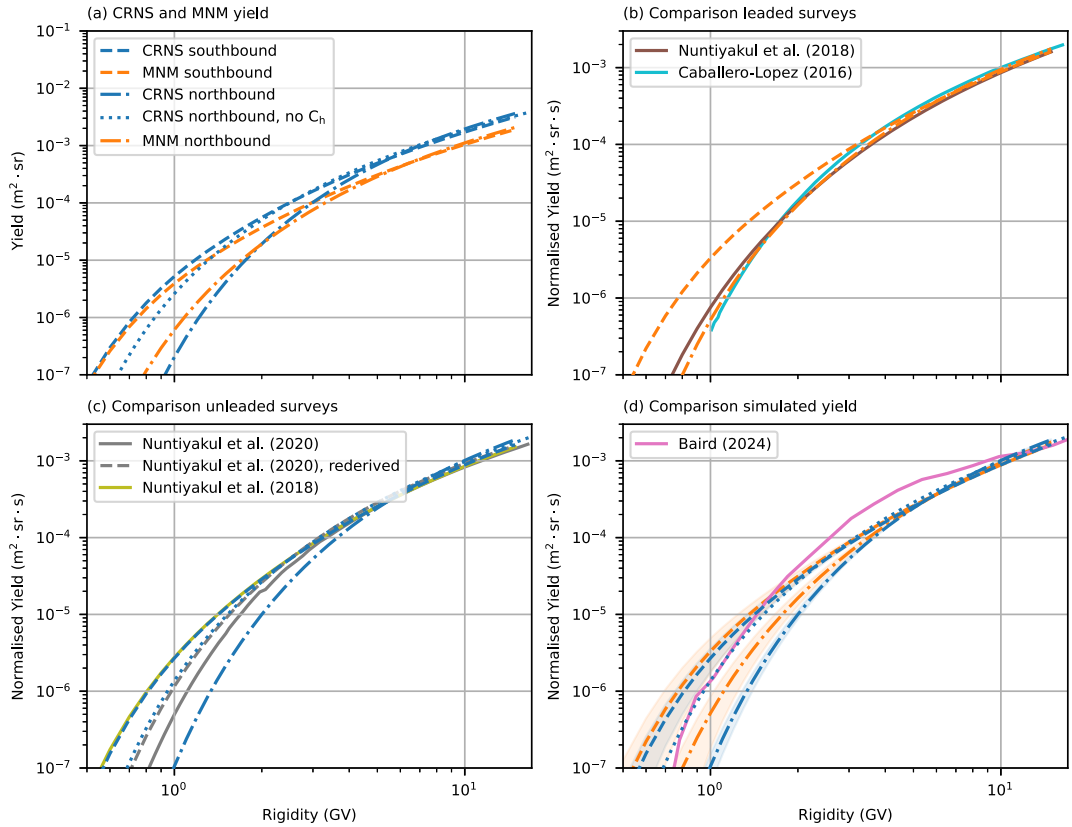


Figure 8. (a) Yield functions of the Quaesta Cosmic Ray Neutron Sensing (CRNS) and mini neutron monitor (MNM). The same yield functions are shown in all panels. (b) Comparison of the MNM yield function to previous leaded neutron detector surveys (Caballero-Lopez, 2016; Nuntiyakul et al., 2018). (c) Comparison of the Quaesta CRNS yield function to previous unleaded but moderated neutron detector surveys (Nuntiyakul et al., 2018, 2020). The CRNS Quaesta yield is also shown without humidity correction (see Section 2.4.3), marked as no C_h. (d) Comparison of MNM and CRNS yield to a simulated yield function taken from Baird (2024), alongside an error of 3σ around the CRNS and MNM yield.

in the shape: while the derived functions show a smooth curve, there is a noticeable knee in the simulated function around 5 GV. Below this knee the two journeys lie on either side of the simulated yield functions.

4. Discussion

The observed difference between the south- and northbound journeys indicates that not all changes between these two journeys have been taken into account. As shown in Figure 4 the largest difference between them is the behavior of the solar modulation potential, exhibiting a much greater variation during the southbound journey. The coefficients of the Dorman function are dependent on the solar modulation. Therefore, strong short term variations in the solar modulation could lead to different Dorman functions being observed at different rigidities. These short term changes in the count rate can not be captured when the data is fit with the Dorman function over an entire journey nor can the primary spectrum (Equation 2) accurately represent them using the mean solar modulation potential of the entire journey. This likely explains why the southbound MNM yield diverges below 5 GV from both the yield function derived by Caballero-Lopez (2016) and the 3NM64 yield function based on Nuntiyakul et al. (2018), while the northbound MNM agrees well with both (Figure 8b). It should also be noted that the overall contribution to neutron monitor count rate from primaries below 3 GV is low (Gieseler et al., 2017), which is precisely the rigidity range where the journey-to-journey differences are largest.

The picture is more nuanced for the CRNS comparison with previous non-leaded surveys (Figure 8c). Above 5 GV all yield functions agree well, which is reassuring given the differences in detector geometry and solar conditions across surveys. Below this threshold, however, the southbound CRNS is consistent with Nuntiyakul et al. (2018) who conducted a 1995 solar minimum survey using a BF_3 counter surrounded by 5 cm of urethane

21699402, 2026, 8, Downloaded from https://agupubs.onlinelibrary.wiley.com/doi/10.1029/2026JA035434 by CochraneItalia, Wiley Online Library on [21/08/2026]. See the Terms and Conditions (https://onlinelibrary.wiley.com/terms-and-conditions) on Wiley Online Library for rules of use; OA articles are governed by the applicable Creative Commons License

21699402, 2026, 8, Downloaded from https://agupubs.onlinelibrary.wiley.com/doi/10.1029/2026JA035434 by CochraneItalia, Wiley Online Library on [21/08/2026]. See the Terms and Conditions (https://onlinelibrary.wiley.com/terms-and-conditions) on Wiley Online Library for rules of use; OA articles are governed by the applicable Creative Commons License

foam. On the other hand, the northbound CRNS diverges from Nuntiyakul et al. (2020), who conducted a survey 2009–2010 utilizing a non-leaded ^{3}He detector moderated by approximately 2.5 cm of paraffin wax, which is geometrically the closest analogue to the Quaesta CRNS among all previous surveys. Disentangling whether the divergence reflects differences in moderator geometry or in the assumed primary spectrum is non-trivial, since Nuntiyakul et al. (2018) used Equation 2 to derive the spectrum while Nuntiyakul et al. (2020) used PAMELA measurements (Adriani et al., 2013).

In order to isolate the spectral contribution, the yield function of Nuntiyakul et al. (2020) was re-derived utilizing Equation 2. This re-derived yield function is closer to Nuntiyakul et al. (2018) but still clearly separated, indicating that both moderator material and thickness and the primary spectrum are of key importance. Importantly, the re-derived Nuntiyakul et al. (2020) agrees well with the northbound CRNS without humidity correction, lending credibility to the northbound results and highlighting that the choice of humidity correction (which is in turn potentially dependent on cut-off rigidity) has a substantial influence on the yield function shape below 5 GV.

The comparison of the derived yield functions and the simulated yield function by Baird (2024) reveals different trajectories (Figure 8d), which may arise from different underlying causes. The most obvious difference between the simulation and reality lies in the environmental response simulation: the simulation considered a CRNS detector surrounded by wet soil, rather than a large ship surrounded by saline water. Additionally, the radiation transport from the top of the atmosphere to an altitude of 200 m was performed with the MAIRE model, which assumes a static, dry atmosphere. There are also assumptions in arriving at the derived yield function which must also be considered, primarily the accuracy of the assumed spectrum, and the ratio of the proton yield function to the alpha yield function. Further work is required to fully understand the discrepancy.

The observed dynamics between the normalized humidity corrected CRNS and MNM contrasts with previously reported differences during solar events, particularly GLEs. During a GLE the primary cosmic ray spectrum experiences an increase of low energy protons. GLE observations in leaded and non-leaded detectors indicate a higher yield for unleaded than leaded detectors in the low energy range (Vashenyuk et al., 2007). The yield functions derived in this work exhibit the opposite behavior, yet they show partial agreement with previous latitude surveys as shown in Figure 8. It should also be noted that the same dynamic of the CRNS and MNM was already seen in the Dorman function (Figure 7) and is therefore not dependent on the derivation of the yield function. It is clear from Figure 8a that the humidity correction has a large influence on the shape of the yield function below approximately 5 GV. A cut-off rigidity dependence of the humidity correction could introduce a significant change in the yield function, as the atmospheric humidity is correlated with latitude, which in turn is correlated with cut-off rigidity. Furthermore, the steel body of the vessel may influence the neutron count rates, through the ship effect (Kouzes et al., 2008). The presence of large masses of an efficient neutron evaporator will change the local neutron field. Therefore, if a neutron detector is placed inside this affected field it will observe a different count rate than if it where placed inside the same environment without the efficient neutron evaporator. This discrepancy is especially strong on ships since iron is an exceedingly efficient neutron evaporator and water an especially poor one. Thus, on a ship at sea, the local neutron field is heavily dependent on the ships ability to evaporate neutrons. If the neutron detector and ship are now observed as one system, then the overall response function of that system will diverge from just the neutron detector over water. This fact can be simply illustrated by comparing the response functions of a neutron monitor and a bare neutron detector (Clem & Dorman, 2000; Millán-Callado et al., 2025). Due to the comparatively thinner shielding and absence of a lead producer it is plausible that a CRNS detector would be more strongly affected by the large iron mass of the ship than the MNM.

The rigidity at which the muon telescope Dorman function plateaus, as shown in Figure 7a, indicates that the minimum rigidity for a primary particle to produce a shower that results in a muon observable at sea level is approximately 4 GV, corresponding to a proton kinetic energy of 3.2 GeV. The origin of this difference between neutron and muon responses is not immediately evident; however, two plausible explanations can be considered, one concerned with muon production and the other with decay in the atmosphere. First, muons are predominantly produced via the decay of charged pions and kaons (Cecchini & Spurio, 2012), which are themselves formed through interactions of primary cosmic rays with atmospheric nuclei. The muon production channel that requires the lowest energy is the decay of a charged pion. In order to estimate the required cosmic ray energy to produce a charged pion, the scattering can be approximated as a proton–proton collision. The lowest-energy channel to produce a charged pion would be $p + p \rightarrow d + \pi^{+}$, whilst for a negatively charged pion $p + p \rightarrow p + p + \pi^{+} + \pi^{-}$. Assuming a fixed target collision and that all secondary particles are at rest, the

21699402, 2026, 8, Downloaded from https://agupubs.onlinelibrary.wiley.com/doi/10.1029/2026JA035434 by CochraneItalia, Wiley Online Library on [21/08/2026]. See the Terms and Conditions (https://onlinelibrary.wiley.com/terms-and-conditions) on Wiley Online Library for rules of use; OA articles are governed by the applicable Creative Commons License

minimum kinetic energies can be calculated from kinematics as $E_{\min} = 0.3$ GeV and $E_{\min} = 0.6$ GeV respectively. The kinetic energies correspond to minimum rigidities of $R_{\min} = 0.8$ GV and $R_{\min} = 1.2$ GV. Whilst both thresholds are close to 1 GV, where neutron observations plateau, they are significantly lower than the muon observation plateau. Second, muons have a shorter mean lifetime compared to neutrons, $2.2 \cdot 10^{-6}$ s and 878.4 s (Navas et al., 2024) respectively. Thus, muon decay is a significant factor in the atmosphere while neutron decay has little influence. Depending on the altitude and angle at which the muon is produced, it may decay before reaching the ground and being detected. The distance a muon can travel is therefore strongly dependent on its Lorentz factor and hence its kinetic energy. Furthermore, as the pion mean lifetime ($2.6 \cdot 10^{-8}$ s) is again much shorter than the muon's (Navas et al., 2024) the distance traveled by the pion before it decays is negligible compared to the distance traveled by the muon. This suggests a mechanism by which the difference between muon and neutron observations in latitude surveys could be explained. At rigidities below approximately 4 GV a primary cosmic ray has a substantially reduced probability of causing a muonic shower energetic enough to reach sea level before the muon decays. If this mechanism is accurate then it has two direct consequences: First, the plateau point should shift toward higher rigidities for obliquely incident muons compared to vertical ones. Second, the plateau point should shift toward lower rigidities as the latitude survey is performed at higher altitudes. The second consequence was reported in Makhmutov et al. (2009), further suggesting the importance of muon decay for the location of the plateau point.

5. Conclusions

This work presents the results of a latitude survey between November 2024 and April 2025, featuring three different neutron detectors and two different muon detectors. Differential response functions for the Quaesta CRNS, MNM, and the muon telescope were derived and compared. The yield functions of the Quaesta CRNS and the MNM were determined and compared with previous latitude surveys.

The derived yield functions from the Quaesta CRNS and MNM detectors exhibited good agreement across a wide range of rigidities. This empirically confirms a long-standing assumption that the signals of both detectors are comparable, that is, usable for applications such as the correction of CRNS data for incoming cosmic rays, using neutron monitor data. However, the results differ for northbound and southbound journeys, which were conducted in the first and second halves of the survey. The yield functions of the CRNS and MNM showed almost perfect agreement during the southbound journey, while the MNM exhibited a higher yield below 5 GV during the northbound journey. Good agreement with previous latitude surveys was found for the yield functions derived from the northbound journey. The northbound MNM yield agrees with two previous surveys using leaded detectors. The northbound CRNS yield also agrees reasonably well with a previous survey of similar detector geometry. This agreement is only valid when the same method is utilized to derive the primary spectrum, highlighting their importance for the derivation of the yield functions. Interestingly, the comparable dynamics between the MNM and CRNS yields are in contrast to previously published yield functions derived from GLE events. This shows that further research is needed to accurately assess the influence of additional effects on unleaded neutron detectors such as the ship effect and the atmospheric corrections.

These results indicate that more sophisticated rescaling methods based on the incoming energy spectrum might be necessary when correcting CRNS data for changes in solar modulation using neutron monitor data. Utilizing the Dorman functions derived during both journey, alongside Equation A1 the required scaling between the MNM and the CRNS can be estimated as a function of cut-off rigidity. The magnitude of this scaling has a maximum of 1.4 % at the highest sampled cut-off rigidity (14.6 GV) and is significantly lower at most other rigidities. This precision is sufficient for most CRNS applications, supporting the assumption made in previous studies that these influences could be neglected for incoming correction methods (McJannet & Desilets, 2023). However, for high-precision applications, further research is needed to gain a more detailed understanding of the yield function variation across the solar cycle.

The largely similar sensitivity between MNM and CRNS lends credibility to the potential use of CRNS detectors for space weather observations, as was suggested by Franz et al. (2025), particularly under hydrologically stable conditions, such as over-water deployments (McJannet et al., 2025; Schrön et al., 2024), indoor settings (Baird et al., 2025), or seasonal Arctic (Riggi et al., 2025) and Antarctic (Hubert, 2024) observations. Large GLEs could also be detected in environments of less hydrological stability, since the signal strength likely overcomes environmental variations on the relevant timescale (Hands et al., 2021).

Regarding muons, the derived differential response function was found to be significantly different from those of the neutron detectors, confirming that muon detectors are more sensitive to higher-energy particles than neutron detectors. This indicates that sophisticated rescaling techniques would be necessary before muon data could be used for the incoming correction of CRNS data.

Appendix A: Correction of CRNS Data With Neutron Monitors and Muon Detectors

Deriving accurate soil moisture estimates from CRNS count rates in the epithermal energy range requires their correction for variations in solar modulation. The most common approach is the use of neutron monitor data (Schrön et al., 2025). Due to the sparse distribution of neutron monitors around the globe, different scaling approaches have been developed to account for differences in cut-off rigidity and atmospheric shielding depth between the CRNS location and the location of the neutron monitor used (Hawdon et al., 2014; Hertle et al., 2025; McJannet & Desilets, 2023; Zreda et al., 2012). All these scaling functions take the general shape

$$N_{\text{corrected}} = N_{\text{observed}} \cdot \left[\tau \cdot \left(\frac{M}{M_{\text{ref}}} - 1\right) + 1\right]^{-1}. \tag{A1}$$

Here M refers to the count rate of a reference monitor and τ to the scaling factor which is specific to each proposed approach. The methods proposed by McJannet and Desilets (2023) and Hertle et al. (2025) derive their scaling parameter utilizing a fraction of Dorman functions modified by the atmospheric depth of both the reference x_M and the CRNS site x_N

$$\tau = \frac{1 - c_0 x_{\text{N}}}{1 - c_0 x_{\text{M}}} \cdot \frac{1 - \exp\left(-\left[c_1 x_{\text{N}} + c_2\right] R_{\text{N}}^{c_3 x_{\text{N}} - c_4}\right)}{1 - \exp\left(-\left[c_1 x_{\text{M}} + c_2\right] R_{\text{M}}^{c_3 x_{\text{M}} - c_4}\right)}. \tag{A2}$$

If the reference cut-off rigidity R_M and atmospheric depth x_M are assumed to be constant then the denominator in Equation A2 can be absorbed into the pre-factor. For the voyage of the RV Polarstern the atmospheric depth can be reasonably approximated as a constant $x_N = 1033\ \text{g} \cdot \text{cm}^{-2}$, such that a Dorman function only dependent on the CRNS site rigidity R_N remains. Thus, the Dorman function that is assumed in both these approaches can be compared to the CRNS Quaesta Dorman function (see Table 2) derived in this work. This comparison is shown in Figure A1. A range of Dorman functions from a multitude of leaded latitude surveys (Allkofer et al., 1969; Caballero-López & Moraal, 2012; Dorman et al., 2000; Kodama & Inoue, 1970; Nuntiyakul et al., 2014, 2018,

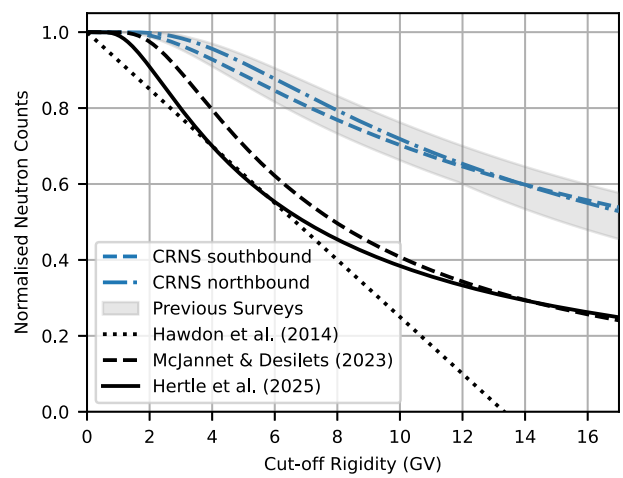


Figure A1. Comparison of Dorman functions taken from McJannet and Desilets (2023), Hertle et al. (2025), Hawdon et al. (2014) and derived from the Cosmic Ray Neutron Sensing (CRNS) Quaesta in this work. A range of Dorman functions is also shown extracted from 21 distinct Dorman coefficient sets taken from Allkofer et al. (1969); Kodama and Inoue (1970); Dorman et al. (2000); Nuntiyakul et al. (2014, 2018, 2025); Caballero-López and Moraal (2012). All of these were derived from leaded latitude surveys. For the CRNS, note that the shown fit extends beyond the rigidity range actually sampled during the survey (0–14.6 GV).

21699402, 2026, 8, Downloaded from https://agupubs.onlinelibrary.wiley.com/doi/10.1029/2026JA035434 by CochraneItalia, Wiley Online Library on [21/08/2026]. See the Terms and Conditions (https://onlinelibrary.wiley.com/terms-and-conditions) on Wiley Online Library for rules of use; OA articles are governed by the applicable Creative Commons License

21699402, 2026, 8, Downloaded from https://agupubs.onlinelibrary.wiley.com/doi/10.1029/2026JA035434 by Cochraneltalia, Wiley Online Library on [21/08/2026]. See the Terms and Conditions (https://onlinelibrary.wiley.com/terms-and-conditions) on Wiley Online Library for rules of use; OA articles are governed by the applicable Creative Commons License

2025) is also included, showing the variability of the Dorman function over multiple solar cycles. Both correction methods display a much steeper decline with rigidity than the parameters sets derived from latitude surveys, either close to the solar minimum or solar maximum. The cause for this discrepancy might lie in the way the correction functions were derived. The functions are numerical fits on data from an ensemble of NM sites, distributed across several atmospheric depths and several decades in time. As a consequence, these Dorman functions are a product of various solar cycles and atmospheric depths, which may explain their difference to latitude surveys at sea level and at a specific point in time.

An alternative approach has been proposed by Stevanato et al. (2022), suggesting the use of muon intensities measured alongside epithermal neutrons at the CRNS location to capture local variations in solar modulation. However, evaluations of this approach were inconclusive (e.g., Gianessi et al., 2024) with different studies suggesting different responses of neutron monitors and muon detectors to space weather events (McJannet et al., 2025; Riggi et al., 2025). The presented latitude survey sheds light on the different responses of neutron and muon detectors to changes in apparent cut-off rigidity as shown in Figure 7. The response of the muon detector is different to the neutron detector. This suggests a different sensitivity to primary cosmic rays. Therefore, it would require a scaling based on geomagnetic cut-off rigidity and solar modulation to utilize muon measurements for CRNS correction. It could be possible to utilize the Dorman function of both the neutron and muon measurement to derive a scaling function, yet as the muon measurements could not be satisfactorily fit utilizing the Dorman function, such a scaling function is not derived in this work.

Conflict of Interest

Gary Womack and Steven Hamann are co-owners of Quaesta Instruments, and the Quaesta CRNS system used in this study was provided as an in-kind contribution. Quaesta Instruments had no role in study design, data analysis and interpretation, or publication decisions. Enrico Gazzola is an employee of Finapp, and the Finapp system used in this study was provided as an in-kind contribution. Finapp had no role in study design, data analysis and interpretation, or publication decisions.

Availability Statement

The raw data from the muon telescope and the MNM are available on the DESY web interface https://cosmicatweb.desy.de/ctplot/, which also allows data analysis. Raw and processed data of all detectors used in this study alongside necessary atmospheric data and computed cut-off rigidities are available from Hertle et al. (2026). Atmospheric data measured aboard the Polarstern RV are available from Schmithüsen (2026). The solar modulation potential is available from Väisänen et al. (2026). OULU neutron monitor data are available from Oulu neutron monitor (n.d.). The Kp-Index can be obtained from Matzka, Bronkalla, et al. (2021). We acknowledge the use of the OTSO tool 1.0.18, the latest version of which can be obtained from Larsen (2026). Map data used for the figures in this study was kindly provided by OpenStreetMap (openstreetmap.org/copyright).

Acknowledgments

The work was funded by the DFG (German Research Foundation) via the project 357874777, research unit FOR 2694 Cosmic Sense. The experiment has been supported by the 21GRD08 SoMMet project, which received funding from the European Partnership on Metrology, co-financed from the European Union's Horizon Europe Research and Innovation Programme and by the Participating States (funder name: European Partnership on Metrology; funder ID: 10.13039/100019599; Grant 21GRD08 SoMMet). This work was also partly supported by the European Research Council Synergy Grant (GERACLE, 101166910, https://doi.org/10.3030/101166910). The Polarstern research vessel and their missions are funded by the German Alfred Wegener Institute, Helmholtz Centre for Polar and Marine Research, Grant AWI_PS146_00. The CRNS detectors used in this study were kindly provided by manufacturers Quaesta Instruments (Tucson, USA) and Finapp S.P.A. (Padova, Italy). We gratefully acknowledge Dr. Ingo Schewe (AWI) for granting permission to do the experiment on the research vessel, and we thank the AWI team in Bremerhaven for their extraordinary support, in particular Ralf Krocker, Stefanie Klüver and Nina Machner. The neutron monitor data used in this study was kindly provided by the Sodankyla Geophysical Observatory of the University of Oulu, Finland (https://cosmicrays.oulu.fi). Open Access funding enabled and organized by Projekt DEAL.

References

Adriani, O., Barbarino, G. C., Bazilevskaya, G. A., Bellotti, R., Bianco, A., Boezio, M., et al. (2013). Cosmic-ray positron energy spectrum measured by Pamela. *Physical Review Letters*, *111*(8), 081102. https://doi.org/10.1103/PhysRevLett.111.081102

Allkofer, O. C., Andresen, R. D., Bagge, E., Dau, W. D., & Funk, H. (1969). Cosmic rays latitude survey at solar minimum. *Tellus*, *21*(3), 443–446. https://doi.org/10.3402/tellusa.v21i3.10101

Andreasen, M., Jensen, K. H., Desilets, D., Franz, T. E., Zreda, M., Bogena, H. R., & Looms, M. C. (2017). Status and perspectives on the cosmic-ray neutron method for soil moisture estimation and other environmental science applications. *Vadose Zone Journal*, *16*(8), 1–11. https://doi.org/10.2136/vzj2017.04.0086

Baird, F. (2024). The potential use of hydrological neutron sensor networks for space weather monitoring. https://doi.org/10.15126/thesis.901065

Baird, F., Ryden, K. A., Lei, F., & Dyer, C. S. (2025). A compact solution for improving the spatial density of observations of large ground level enhancements. *Space Weather*, *23*(5), e2024SW004230. https://doi.org/10.1029/2024SW004230

Bogena, H. R., Schrön, M., Jakobi, J., Ney, P., Zacharias, S., Andreasen, M., et al. (2022). Cosmos-Europe: A European network of cosmic-ray neutron soil moisture sensors. *Earth System Science Data*, *14*(3), 1125–1151. https://doi.org/10.5194/essd-14-1125-2022

Boschini, M. J., Torre, S. D., Gervasi, M., Grandi, D., Jóhannesson, G., Vacca, G. L., et al. (2020). Inference of the local interstellar spectra of cosmic-ray nuclei $Z \leq 28$ with the GalProp-HelMod framework. *Astrophysical Journal Supplement Series*, *250*(2), 27. https://doi.org/10.3847/1538-4365/aba901

Caballero-Lopez, R. (2016). An estimation of the yield and response functions for the mini neutron monitor. *Journal of Geophysical Research: Space Physics*, *121*(8), 7461–7469. https://doi.org/10.1002/2016JA022690

Caballero-López, R. A., & Moraal, H. (2012). Cosmic-ray yield and response functions in the atmosphere. *Journal of Geophysical Research*, *117*(A12). https://doi.org/10.1029/2012JA017794

Carmichael, H., Bercovitch, M., Steljes, J., & Magidin, M. (1969). I. Cosmic-ray latitude survey in North America in summer, 1965. *Canadian Journal of Physics*, *47*(19), 2037–2050. https://doi.org/10.1139/p69-257

Cecchini, S., & Spurio, M. (2012). Atmospheric muons: Experimental aspects. *Geoscientific Instrumentation, Methods and Data Systems*, *1*(2), 185–196. https://doi.org/10.5194/gi-1-185-2012

Clem, J. M., & Dorman, L. I. (2000). Neutron monitor response functions. *Space Science Reviews*, *93*(1–2), 335–359. https://doi.org/10.1023/A:1026508915269

Cooke, D., Humble, J., Shea, M., Smart, D., Lund, N., Rasmussen, I., et al. (1991). On cosmic-ray cut-off terminology. *Il Nuovo Cimento - B C*, *14*(3), 213–234. https://doi.org/10.1007/BF02509357

de Mendonça, R. R. S., Braga, C. R., Echer, E., Dal Lago, A., Munakata, K., Kuwabara, T., et al. (2016). The temperature effect in secondary cosmic rays (muons) observed at the ground: Analysis of the global muon detector network data. *The Astrophysical Journal*, *830*(2), 88. https://doi.org/10.3847/0004-637x/830/2/88

Desilets, D., & Zreda, M. (2003). Spatial and temporal distribution of secondary cosmic-ray nucleon intensities and applications to in situ cosmogenic dating. *Earth and Planetary Science Letters*, *206*(1–2), 21–42. https://doi.org/10.1016/S0012-821X(02)01088-9

Dorman, L. I. (2004). *Cosmic rays in the earth's atmosphere and underground*. Springer. https://doi.org/10.1007/978-1-4020-2113-8

Dorman, L. I., Villoresi, G., Iucci, N., Parisi, M., Tyasto, M. I., Danilova, O. A., & Ptitsyna, N. G. (2000). Cosmic ray survey to Antarctica and coupling functions for neutron component near solar minimum (1996–1997): 3. Geomagnetic effects and coupling functions. *Journal of Geophysical Research*, *105*(A9), 21047–21056. https://doi.org/10.1029/2000JA900051

Dunai, T. J. (2000). Scaling factors for production rates of in situ produced cosmogenic nuclides: A critical reevaluation. *Earth and Planetary Science Letters*, *176*(1), 157–169. https://doi.org/10.1016/S0012-821X(99)00310-6

Evans, J. G., Ward, H. C., Blake, J. R., Hewitt, E. J., Morrison, R., Fry, M., et al. (2016). Soil water content in southern England derived from a cosmic-ray soil moisture observing system–cosmos-uk. *Hydrological Processes*, *30*(26), 4987–4999. https://doi.org/10.1002/hyp.10929

Franz, T., Desilets, D., Schrön, M., Baird, F., & McJannet, D. (2025). Two neutron-monitoring networks are better than one. *Eos*, *106*. https://doi.org/10.1029/2025EO250212

Gianessi, S., Polo, M., Stevanato, L., Lunardon, M., Francke, T., Oswald, S. E., et al. (2024). Testing a novel sensor design to jointly measure cosmic-ray neutrons, muons and gamma rays for non-invasive soil moisture estimation. *Geoscientific Instrumentation, Methods and Data Systems*, *13*(1), 9–25. https://doi.org/10.5194/gi-13-9-2024

Gieseler, J., Heber, B., & Herbst, K. (2017). An empirical modification of the force field approach to describe the modulation of galactic cosmic rays close to Earth in a broad range of rigidities. *Journal of Geophysical Research: Space Physics*, *122*(11), 10964–10979. https://doi.org/10.1002/2017JA024763

Gleeson, L., & Urch, I. (1973). A study of the force-field equation for the propagation of galactic cosmic rays. *Astrophysics and Space Science*, *25*(2), 387–404. https://doi.org/10.1007/BF00649180

Hands, A. D., Baird, F., Ryden, K., Dyer, C., Lei, F., Evans, J., et al. (2021). Detecting ground level enhancements using soil moisture sensor networks. *Space Weather*, *19*(8), e2021SW002800. https://doi.org/10.1029/2021SW002800

Hands, A. D., Lei, F., Davis, C. S., Clewer, B. J., Dyer, C. S., & Ryden, K. A. (2022). A new model for nowcasting the aviation radiation environment with comparisons to in situ measurements during gles. *Space Weather*, *20*, e2022SW003155. https://doi.org/10.1029/2022SW003155

Hanfland, C., & Cornish, N. (2025). The expeditions ps145/1 and ps145/2 of the research vessel polarstern to the Atlantic Ocean in 2024. *Alfred-Wegener-Institut Helmholtz-Zentrum für Polar- und Meeresforschung*, *795*. https://doi.org/10.57738/BzPM_0795_2025

Hawdon, A., McJannet, D., & Wallace, J. (2014). Calibration and correction procedures for cosmic-ray neutron soil moisture probes located across Australia. *Water Resources Research*, *50*(6), 5029–5043. https://doi.org/10.1002/2013wr015138

Heber, B., Galsdorf, D., Herbst, K., Gieseler, J., Labrenz, J., Schwerdt, C., et al. (2015). Mini neutron monitor measurements at the Neumayer III station and on the German research vessel polarstern. *Journal of Physics: Conference Series*, *632*, 012057. https://doi.org/10.1088/1742-6596/632/1/012057

Hertle, L., Heber, B., Walter, M., Schattan, P., Landmark, S., Womack, G., et al. (2026). Multi detector latitude survey aboard the rv polarstern [Dataset]. *Zenodo*. https://doi.org/10.5281/zenodo.19109381

Hertle, L., Zacharias, S., Larsen, N., Rasche, D., McJannet, D., & Schrön, M. (2025). Neutron monitor based incoming flux correction for cosmic-ray neutron sensing of environmental water. *Water Resources Research*, *61*(9), e2025WR040527. https://doi.org/10.1029/2025WR040527

Hubert, G. (2024). Analyses of continuous measurements of cosmic ray induced-neutrons spectra at the Concordia Antarctic station from 2016 to 2024. *Astroparticle Physics*, *159*, 102949. https://doi.org/10.1016/j.astropartphys.2024.102949

Hubert, G., Herbert, G., Tilhac, A., Rey, R., & Bourlès, B. (2026). Analysis of cosmic ray-induced neutron spectra recorded during Pirata oceanographic cruises. *Journal of Atmospheric and Solar-Terrestrial Physics*, *278*, 106690. https://doi.org/10.1016/j.jastp.2025.106690

Jha, B. K., & Upton, L. A. (2024). Predicting the timing of the solar cycle 25 polar field reversal. *The Astrophysical Journal Letters*, *962*(1), L15. https://doi.org/10.3847/2041-8213/ad20d2

Knust, R. (2017). Polar research and supply vessel polarstern operated by the Alfred-Wegener-institute. *Journal of Large-Scale Research Facilities*, *3*, A119. https://doi.org/10.17815/jlsrf-3-163

Kobelev, P., Belov, A., Mavromichalaki, E., Gerontidou, M., & Yanke, V. (2011). Variations of barometric coefficients of the neutron component in the 22-23 cycles of solar activity. *11*, 382–385. https://doi.org/10.7529/ICRC2011/V11/0654

Kodama, M., & Inoue, A. (1970). Availability and limitation of multiplicity measurements in the nm-64 neutron monitor at Syowa station, Antarctica. JARE scientific reports. *Series A, Aeronomy*, *9*, 1–40.

Köhli, M. (2025). Soil moisture measurements by Cosmic-ray neutron sensing: A critical review. *SSRN Electronic Journal*. https://doi.org/10.2139/ssrn.5404891

Köhli, M., Schrön, M., & Schmidt, U. (2018). Response functions for detectors in cosmic ray neutron sensing. *Nuclear Instruments and Methods in Physics Research Section A: Accelerators, Spectrometers, Detectors and Associated Equipment*, *902*, 184–189. https://doi.org/10.1016/j.nima.2018.06.052

Köhli, M., Schrön, M., Zreda, M., Schmidt, U., Dietrich, P., & Zacharias, S. (2015). Footprint characteristics revised for field-scale soil moisture monitoring with cosmic-ray neutrons. *Water Resources Research*, *51*(7), 5772–5790. https://doi.org/10.1002/2015wr017169

Köhli, M., Weimar, J., Schrön, M., Baatz, R., & Schmidt, U. (2021). Soil moisture and air humidity dependence of the above-ground cosmic-ray neutron intensity. *Frontiers in Water*, *2*, 544847. https://doi.org/10.3389/frwa.2020.544847

Koldobskiy, S. A., Bindi, V., Corti, C., Kovaltsov, G. A., & Usoskin, I. G. (2019). Validation of the neutron monitor yield function using data from ams-02 experiment, 2011–2017. *Journal of Geophysical Research: Space Physics*, *124*(4), 2367–2379. https://doi.org/10.1029/2018JA026340

21699402, 2026, 8, Downloaded from https://agupubs.onlinelibrary.wiley.com/doi/10.1029/2026JA035434 by CochraneItalia, Wiley Online Library on [21/08/2026]. See the Terms and Conditions (https://onlinelibrary.wiley.com/terms-and-conditions) on Wiley Online Library for rules of use; OA articles are governed by the applicable Creative Commons License

Kouzes, R. T., Ely, J. H., Seifert, A., Siciliano, E. R., Weier, D. R., Windsor, L. K., et al. (2008). Cosmic-ray-induced ship-effect neutron measurements and implications for cargo scanning at borders. *Nuclear Instruments and Methods in Physics Research Section A: Accelerators, Spectrometers, Detectors and Associated Equipment*, *587*(1), 89–100. https://doi.org/10.1016/j.nima.2007.12.031

Larsen, N. (2026). Otso: Open-source geomagnetosphere propagation tool [Software]. *Zenodo*. https://doi.org/10.5281/zenodo.15341361

Larsen, N., Mishev, A., & Usoskin, I. (2023). A new open-source geomagnetosphere propagation tool (otso) and its applications. *Journal of Geophysical Research: Space Physics*, *128*(3), e2022JA031061. https://doi.org/10.1029/2022JA031061

Lei, F., Clucas, S., Dyer, C., & Truscott, P. (2004). An atmospheric radiation model based on response matrices generated by detailed monte carlo simulations of cosmic ray interactions. *IEEE Transactions on Nuclear Science*, *51*(6), 3442–3451. https://doi.org/10.1109/TNS.2004.839131

Makhmutov, V., Stozhkov, Y. I., Bazilevskaya, G., Svirzhevsky, N., & Morzabayev, A. (2009). Latitude effect of muons in the earth's atmosphere during solar activity minimum. *Bulletin of the Russian Academy of Sciences: Physics*, *73*(3), 350–352. https://doi.org/10.3103/S1062873809030216

Mangeard, P.-S., Clem, J., Evenson, P., Pyle, R., Mitthumsiri, W., Ruffolo, D., et al. (2018). Distinct pattern of solar modulation of galactic cosmic rays above a high geomagnetic cutoff rigidity. *The Astrophysical Journal*, *858*(1), 43. https://doi.org/10.3847/1538-4357/aabd3c

Matzka, J., Bronkalla, O., Tornow, K., Elger, K., & Stolle, C. (2021). Geomagnetic kp index [Dataset]. *GFZ Data Services*. https://doi.org/10.5880/Kp.0001

Matzka, J., Stolle, C., Yamazaki, Y., Bronkalla, O., & Morschhauser, A. (2021). The geomagnetic kp index and derived indices of geomagnetic activity. *Space Weather*, *19*(5), e2020SW002641. https://doi.org/10.1029/2020SW002641

McJannet, D., & Desilets, D. (2023). Incoming neutron flux corrections for cosmic-ray soil and snow sensors using the global neutron monitor network. *Water Resources Research*, *59*(4), e2022WR033889. https://doi.org/10.1029/2022WR033889

McJannet, D., Rasche, D., Marano, J., Hawdon, A., Stenson, M., & Schrön, M. (2025). Over-water low-energy neutron observations for intensity corrections across cosmic-ray soil moisture sensor networks. *Water Resources Research*, *61*(9), e2024WR039727. https://doi.org/10.1029/2024WR039727

Mendonça, R. R. S., Wang, C., Braga, C., Echer, E., Dal Lago, A., Costa, J., et al. (2019). Analysis of cosmic rays' atmospheric effects and their relationships to cutoff rigidity and zenith angle using global muon detector network data. *Journal of Geophysical Research: Space Physics*, *124*(12), 9791–9813. https://doi.org/10.1029/2019JA026651

Millán-Callado, M. Á., Méndez Villafañe, R., Adam, B. A., Blahušiak, P., Di Chicco, A., Dietz, M., et al. (2025). Response characterization of cosmic-ray neutron sensors in neutron metrology reference fields. *EGUsphere*. https://doi.org/10.5194/egusphere-2025-4825

Mishev, A. L., Koldobskiy, S. A., Kovaltsov, G. A., Gil, A., & Usoskin, I. G. (2020). Updated neutron-monitor yield function: Bridging between in situ and ground-based cosmic ray measurements. *Journal of Geophysical Research: Space Physics*, *125*(2), e2019JA027433. https://doi.org/10.1029/2019JA027433

Moraal, H. (2013). Cosmic-ray modulation equations. *Space Science Reviews*, *176*(1–4), 299–319. https://doi.org/10.1007/s11214-011-9819-3

Moraal, H., Belov, A., & Clem, J. M. (2000). Design and co-Ordination of multi-station international neutron monitor networks. *Space Science Reviews*, *93*(1), 285–303. https://doi.org/10.1023/A:1026504814360

Nagashima, K., Sakakibara, S., Murakami, K., & Morishita, I. (1989). Response and yield functions of neutron monitor, galactic cosmic-ray spectrum and its solar modulation, derived from all the available world-wide surveys. *Il Nuovo Cimento - B C*, *12*(2), 173–209. https://doi.org/10.1007/BF02523790

Navas, S., Amsler, C., Gutsche, T., Hanhart, C., Hernández-Rey, J. J., Lourenço, C., et al. (2024). Review of particle physics. *Physics Review D*, *110*(3), 030001. https://doi.org/10.1103/PhysRevD.110.030001

Nuntiyakul, W., Evenson, P., Ruffolo, D., Saiz, A., Bieber, J. W., Clem, J., et al. (2014). Latitude survey investigation of galactic cosmic ray solar modulation during 1994–2007. *The Astrophysical Journal*, *795*(1), 11. https://doi.org/10.1088/0004-637X/795/1/11

Nuntiyakul, W., Mangeard, P.-S., Ruffolo, D., Evenson, P., Bieber, J. W., Clem, J., et al. (2020). Direct determination of a bare neutron counter yield function. *Journal of Geophysical Research: Space Physics*, *125*(4), e2019JA027304. https://doi.org/10.1029/2019JA027304

Nuntiyakul, W., Promfu, T., Seripienlert, A., Khamphakdee, S., Pagwhan, A., Sohn, J., et al. (2025). Response functions of a neutron monitor from the 2023-24 latitude survey aboard the Araon icebreaker. In *39th international cosmic ray conference (icrc2025)*. https://doi.org/10.22323/1.501.1348

Nuntiyakul, W., Sáiz, A., Ruffolo, D., Mangeard, P.-S., Evenson, P., Bieber, J., et al. (2018). Bare neutron counter and neutron monitor response to cosmic rays during a 1995 latitude survey. *Journal of Geophysical Research: Space Physics*, *123*(9), 7181–7195. https://doi.org/10.1029/2017JA025135

Oulu neutron monitor (n.d.). Sodankyla geophysical observatory [Dataset]. https://cosmicrays.oulu.fi/

Poluianov, S., & Batalla, O. (2022). Cosmic-ray atmospheric cutoff energies of polar neutron monitors. *Advances in Space Research*, *70*(9), 2610–2617. https://doi.org/10.1016/j.asr.2022.03.037

Poopakun, K., Nuntiyakul, W., Kato, C., Munakata, K., Kozai, M., Hayashi, Y., et al. (2025). Solar and interplanetary determinants of long-term solar modulation of cosmic-ray intensity for median rigidities of 11–107 gv. *The Astrophysical Journal*, *991*(2), 127. https://doi.org/10.3847/1538-4357/adfdd3

Potgieter, M. S. (2013). Solar modulation of cosmic rays. *Living Reviews in Solar Physics*, *10*, 1–66. https://doi.org/10.12942/lrsp-2013-3

Riggi, F., Hertle, L., Abbrescia, M., Avanzini, C., Baldini, L., Baldini Ferroli, R., et al. (2025). High latitude observation of the Forbush decrease during the May 2024 solar storms with muon and neutron detectors on Svalbard. *Advances in Space Research*, *76*(2), 1225–1239. https://doi.org/10.1016/j.asr.2025.05.023

Rosolem, R., Shuttleworth, W., Zreda, M., Franz, T. E., Zeng, X., & Kurc, S. (2013). The effect of atmospheric water vapor on neutron count in the cosmic-ray soil moisture observing system. *Journal of Hydrometeorology*, *14*(5), 1659–1671. https://doi.org/10.1175/JHM-D-12-0120.1

Ruffolo, D., Saiz, A., Mangeard, P.-S., Kamyan, N., Muangha, P., Nutaro, T., et al. (2016). Monitoring short-term cosmic-ray spectral variations using neutron monitor time-delay measurements. *The Astrophysical Journal*, *817*(1), 38. https://doi.org/10.3847/0004-637X/817/1/38

Schmithüsen, H. (2026). Continuous meteorological surface measurement during polarstern cruises [Dataset]. *PANGAEA*. https://doi.org/10.1594/PANGAEA.995326

Schrön, M., Köhli, M., Scheiffele, L., Iwema, J., Bogena, H. R., Lv, L., et al. (2017). Improving calibration and validation of cosmic-ray neutron sensors in the light of spatial sensitivity. *Hydrology and Earth System Sciences*, *21*(10), 5009–5030. https://doi.org/10.5194/hess-21-5009-2017

Schrön, M., Köhli, M., & Zacharias, S. (2023). Signal contribution of distant areas to cosmic-ray neutron sensors – Implications for footprint and sensitivity. *Hydrology and Earth System Sciences*, *27*(3), 723–738. https://doi.org/10.5194/hess-27-723-2023

Schrön, M., Rasche, D., Weimar, J., Köhli, M., Herbst, K., Boehrer, B., et al. (2024). Buoy-based detection of low-energy cosmic-ray neutrons to monitor the influence of atmospheric, geomagnetic, and heliospheric effects. *Earth and Space Science*, *11*(6), e2023EA003483. https://doi.org/10.1029/2023EA003483

21699402, 2026, 8, Downloaded from https://agupubs.onlinelibrary.wiley.com/doi/10.1029/2026JA035434 by CochraneItalia, Wiley Online Library on [21/08/2026]. See the Terms and Conditions (https://onlinelibrary.wiley.com/terms-and-conditions) on Wiley Online Library for rules of use; OA articles are governed by the applicable Creative Commons License

Schrön, M., Zacharias, S., Baatz, R., Baroni, G., Bogena, H., Brogi, C., et al. (2025). *Global cosmos reference (draft)*. Zenodo. https://doi.org/10.5281/zenodo.17959506

Simpson, J. (1983). Elemental and isotopic composition of the galactic cosmic rays. *Annual Review of Nuclear and Particle Science*, *33*(1), 323–382. https://doi.org/10.1146/annurev.ns.33.120183.001543

Stevanato, L., Baroni, G., Cohen, Y., Fontana, C. L., Gatto, S., Lunardon, M., et al. (2019). A novel cosmic-ray neutron sensor for soil moisture estimation over large areas. *Agriculture*, *9*(9), 202. https://doi.org/10.3390/agriculture9090202

Stevanato, L., Baroni, G., Oswald, S. E., Lunardon, M., Mares, V., Marinello, F., et al. (2022). An alternative incoming correction for cosmic-ray neutron sensing observations using local muon measurement. *Geophysical Research Letters*, *49*(6), e2021GL095383. https://doi.org/10.1029/2021GL095383

Stoker, P., van der Walt, A., Potgieter, M., & Martin, R. (1980). Modulation of cosmic rays during solar minimum. Part 1. Cosmic ray intensity survey at sea-level during 1976: Experimental details. *South African Journal of Physics*, *3*(3–4), 73–76.

Strauss, D. T., Poluianov, S., Van Der Merwe, C., Krüger, H., Diedericks, C., Krüger, H., et al. (2020). The mini-neutron monitor: A new approach in neutron monitor design. *Journal of Space Weather and Space Climate*, *10*(39), 39. https://doi.org/10.1051/swsc/2020038

Tanaka, H. K. M. (2025). Distance of flight of cosmic-ray muons to study dynamics of the upper Muosphere. *Geoscientific Instrumentation, Methods and Data Systems*, *14*(1), 1–11. https://doi.org/10.5194/gi-14-1-2025

Tirado-Bueno, E., Mendoza-Torres, J. E., & de Mendonça, R. R. (2021). Barometric coefficient dependence on the geomagnetic cutoff rigidity of neutron monitors. *Advances in Space Research*, *68*(6), 2631–2642. https://doi.org/10.1016/j.asr.2021.04.034

Tsyganenko, N. (1989). A magnetospheric magnetic field model with a warped tail current sheet. *Planetary and Space Science*, *37*(1), 5–20. https://doi.org/10.1016/0032-0633(89)90066-4

Väisänen, P., Larsen, N., Koldobskiy, S., Similä, M., Pelosi, D., & Orcinha, M. (2026). Near-earth modulation (nem) index in 1-hour resolution [Dataset]. https://doi.org/10.23729/fd-a60b9049-249c-36f9-862f-5772f9ace862

Väisänen, P., Usoskin, I., & Mursula, K. (2021). Seven decades of neutron monitors (1951–2019): Overview and evaluation of data sources. *Journal of Geophysical Research: Space Physics*, *126*(5), e2020JA028941. https://doi.org/10.1029/2020JA028941

Vashenyuk, E., Balabin, Y., & Stoker, P. (2007). Responses to solar cosmic rays of neutron monitors of a various design. *Advances in Space Research*, *40*(3), 331–337. https://doi.org/10.1016/j.asr.2007.05.018

Verpoest, S., Soldin, D., & Desiati, P. (2024). Atmospheric muons and their variations with temperature. *Astroparticle Physics*, *161*, 102985. https://doi.org/10.1016/j.astropartphys.2024.102985

Villoresi, G., Dorman, L. I., Iucci, N., & Ptitsyna, N. G. (2000). Cosmic ray survey to Antarctica and coupling functions for neutron component near solar minimum (1996–1997): 1. Methodology and data quality assurance. *Journal of Geophysical Research*, *105*(A9), 21025–21034. https://doi.org/10.1029/2000JA900048

Vos, E. E., & Potgieter, M. S. (2015). New modeling of galactic proton modulation during the minimum of solar cycle 23/24. *The Astrophysical Journal*, *815*(2), 119. https://doi.org/10.1088/0004-637X/815/2/119

Vykydal, Z., Šolc, J., Rusňák, J., Blahušiak, P., Vlk, P., Köhli, M., et al. (2025). Monte Carlo simulation and experimental validation of the finapp model 3 cosmic-ray neutron sensor. *Measurement Science and Technology*, *37*(1), 015901. https://doi.org/10.1088/1361-6501/ae2649

Walter, M., Gnebner, C., Heber, B., Herbst, K., Krüger, H., Krüger, H. G., et al. (2024). Measurements of cosmic rays by a mini-neutron monitor at Neumayer III from 2014 to 2017. *Space Weather*, *22*(6), e2023SW003596. https://doi.org/10.1029/2023SW003596

Weimar, J. (2022). *Advances in cosmic-ray neutron sensing by Monte Carlo simulations and neutron detector development*. Heidelberg University. https://doi.org/10.11588/heidok.00032046

Zreda, M., Desilets, D., Ferré, T. P. A., & Scott, R. L. (2008). Measuring soil moisture content non-invasively at intermediate spatial scale using cosmic-ray neutrons. *Geophysical Research Letters*, *35*(21). https://doi.org/10.1029/2008GL035655

Zreda, M., Shuttleworth, W. J., Zeng, X., Zweck, C., Desilets, D., Franz, T., & Rosolem, R. (2012). COSMOS: The COsmic-ray soil moisture observing system. *Hydrology and Earth System Sciences*, *16*(11), 4079–4099. https://doi.org/10.5194/hess-16-4079-2012

21699402, 2026, 8, Downloaded from https://agupubs.onlinelibrary.wiley.com/doi/10.1029/2026JA035434 by CochraneItalia, Wiley Online Library on [21/08/2026]. See the Terms and Conditions (https://onlinelibrary.wiley.com/terms-and-conditions) on Wiley Online Library for rules of use; OA articles are governed by the applicable Creative Commons License